Frequency Response Simulations and Tests of an Aeroservoelastic Wind Tunnel Model

Alison Zongolowicz

A thesis
submitted in partial fulfillment of the
requirements for the degree of

Master of Science

University of Washington

2019

Reading Committee:

Eli Livne, Chair

Mehran Mesbahi

Program Authorized to Offer Degree:
Aeronautics and Astronautics

University of Washington

Abstract

Frequency Response Simulations and Tests of an Aeroservoelastic Wind Tunnel Model

Alison Zongolowicz

Chair of the Supervisory Committee:
Professor Eli Livne
Aeronautics and Astronautics

The development of active controls has the potential to provide weight savings, cost savings, and safety enhancements for many types of aircraft. With the creation of an aeroservoelastic wind tunnel model and testbed, the William E. Boeing Department of Aeronautics and Astronautics now has the capability to test active controls on representative flexible aircraft configurations. Simulations of the aeroservoelastic model, validated by experimental data, advance the field of active controls by establishing reference test cases that are ready for testing alternative active control laws. This thesis focuses on frequency response simulations that use inputs from a NASTRAN Finite Element Model to create a state-space representation that aids in modern control law design for Active Flutter Suppression. Two analytical-numerical methods for finding the frequency response of the model are used and compared to one another as well as to experimental data to produce a full aeroservoelastic wind tunnel model test case.

TABLE OF CONTENTS

Page

List of Figures iii

List of Tables v

Chapter 1: Introduction 1
1.1 Background 1
1.2 Motivation 2
1.3 Challenges 2
1.4 Needs and Contributions 4

Chapter 2: Mathematical Modeling of Frequency Response Methods 7
2.1 Second-order Method 8
2.2 First-order Method 9

Chapter 3: Simulation Capability 21
3.1 NASTRAN Model 21
3.2 MATLAB Simulation 23

Chapter 4: Test Case 25
4.1 Test Article 26
4.2 Wind Tunnel 30
4.3 Test Techniques 32

Chapter 5: Analytical Predictions 37
5.1 Roger Approximation 37
5.2 Flutter Prediction 38

5.3 Initial Frequency Response Results 39

Chapter 6: Technical Discussion 42
6.1 Initial Comparisons 42
6.2 Fine-tuning of the Simulation Codes 43
6.3 Additional Comparisons 48
6.4 Other Observations 51

Chapter 7: Conclusion 53

Bibliography 54

Appendix A: Simulation Flowchart 56

Appendix B: Flutter Prediction Methods 57
B.1 Ug Method 57
B.2 Root Locus Method 59

LIST OF FIGURES

Figure Number Page

3.1 Structural elements of the finite element model. 21
3.2 Aero-structural finite element model. 22

4.1 Wind tunnel testbed sideview. 25
4.2 Overall test article assembly. 27
4.3 Signals used for servo system identification. 31
4.4 Estimated frequency response function and candidate transfer functions. 32
4.5 Result of preliminary two-dimensional steady gust vane effect analysis. 33
4.6 Configuration of the test article and mounting equipment in the context of the wind tunnel test section. 34
4.7 Changes in first wing bending damping due to foam and tip mass. 35
4.8 Time histories of input and measurement signals used in dwell tests for identification of first wing bending damping ratio. 36

5.1 Comparison of Roger approximation values to actual values 37
5.2 Ug method flutter analysis. 39
5.3 Result of root locus flutter analysis. 40
5.4 Second-order method results. 41
5.5 First-order method results. 41

6.1 Comparison of both methods. 43
6.2 Comparison of simulations to experimental data before accounting for damping, aerodynamic efficiency, and root gap effects. 44
6.3 Aerodynamic correction factors. 45
6.4 Added structural damping of $\zeta = 0.02$. 46
6.5 Responses with varying added structural damping. 48
6.6 Effect of adding hinge friction damping. 49

6.7 Comparison of simulations done using different methods of aerodynamic analysis. 50
6.8 Effect of addition of ceiling gap in simulated data. 50
6.9 Accelerometer transfer function. 51
6.10 Frequency response up to 25 Hz. 52

A.1 Flowchart of MATLAB simulation. 56

LIST OF TABLES

Table Number Page

2.1 Equation variable descriptions. 7

3.1 User-defined required simulation inputs. 23

4.1 Desired aero-structural characteristics for test case. 28

4.2 Overview of structural components. 29

4.3 MKS HV6130 wing servo specified characteristics. 30

5.1 Flutter prediction values. 38

ACKNOWLEDGMENTS

The author wishes to express sincere appreciation to her advisor, Eli Livne, for all of his time, effort, and guidance. She would also like to thank the UWAA-Boeing Controls Team: Jake Quenzer, Kimber Hinson, Bijan Barzgaran, Kristi Morgansen, and Mehran Mesbahi. The collaborative effort of this team is what created MARGE and the experimental results used in this thesis. She would also like to thank Marat Mor for his assistance during the creation of this thesis. She would like to thank her family and friends for their encouragement and support throughout all of graduate school. She is also grateful to the Federal Aviation Administration for funding her work.

Chapter 1

INTRODUCTION

1.1 Background

Aeroelasticity involves the interaction of steady and unsteady aerodynamic forces and the structural dynamics of aircraft. Within aeroelasticity, flutter is a self-excited instability driven by the interplay of structural deformations and corresponding aerodynamic loads. Flutter can be categorized based on type and intensity of how stability is lost. The most severe types of flutter can have catastrophic effects. Explosive divergent flutter is caused by a slight increase in speed, which can change the stability of the aeroelastic system from very stable to highly unstable. This can lead to airframe failure within a fraction of a second. Since flutter deals with a loss in stability and can sometimes lead to failure, aircraft are typically designed to have flutter far beyond their flight envelopes. In order to meet this requirement, the airframe must have certain structural dynamic properties, which often mean increased weight. However, if active controls can be allowed to stabilize flutter mechanisms within the flight envelope, then the airframe may be designed to be lighter in weight, leading to major benefits.

Active controls have been heavily researched in the recent years within the aerospace field. This includes a number of categories that have already been certified and are in use, including maneuver load control, gust load alleviation, active ride comfort systems, and systems for desired and safe handling qualities. The type of active control that would suppress flutter within the flight envelope is known as Active Flutter Suppression (AFS). AFS works to suppress instabilities associated with flutter through the closed-loop action of control surfaces. Potentially catastrophic consequences of

AFS failure and the unstable nature of the uncontrolled system are among the many challenging problems which must be addressed for AFS systems before their benefits can be fully realized.

1.2 Motivation

The principal benefit of AFS is weight savings. The ability to design the structural aspects of an aircraft without ”pushing” flutter to be outside the flight envelope allows for structural optimization to reduce airframe weight. These weight savings lead to better efficiency, and, because of the relaxed constraint on the flutter region, would allow for more versatility in airframe design.

Weight savings may be a significant benefit resulting from the inclusion of AFS at the start of the design of an aircraft. However, AFS can also be beneficial to remedy aeroelastic problems that arise late in development, where typical passive modifications are not cost or schedule acceptable. Still, challenges presented by aircraft dynamics, control law synthesis, math modeling, testing, and certification are preventing AFS technology from being fully realized.

1.3 Challenges

One of the first challenges involved with AFS is the accuracy of the math model that represents the system dynamics. For example, capturing static aeroelastic effects on dynamic aeroelastic behaviors is a problem when formulating the equations of motion of the aircraft. Typically such effects are accounted for in the field of 6 degrees of freedom flight dynamics by static aeroelastic corrections of aerodynamic stability derivatives, where the corrections and stability derivatives are determined through simulations. Advances made in finite element modeling and unsteady linear aerodynamics have contributed to the capability to model deformable airplanes in flight, including their 6 degree-of-freedom (DOF) ”rigid body” motions and the elastic deformations. The rigid body / elastic deformation motions are typically modeled, using a Lagrangian approach, by a superposition of pre-selected deformation mode shapes. Thus both static and dynamic aeroelastic behaviors can be accurately captured by the resulting math models.

Now, from a control law synthesis perspective mathematical models of the "plant" to be controlled should, desirably, be as low order as possible. For AFS, making sure that all important static and dynamic aeroelastic modes of behaviors are accurately captured in a reduced-order model is essential to the development and validation of appropriate controllers.

Along with challenges in the synthesis of the AFS control law, there are also challenges due to the integration of AFS with other active control systems on an aircraft. If not adequately considered, interference between different control systems on an aircraft can have unfavorable effects. Historically, strong interactions between control systems of deformable flight vehicles have been prevented due to differences in the frequency bands in which the different control laws operated and due to hardware limitations such as frequency response, power, and rate limitations of actuators. Relatively slow actuators were sufficient for controlling rigid-body dynamics of the aircraft when lowest frequency modes of vibration were much higher in frequency than the flight dynamic poles of the "rigid" airplane. Such control systems were consequently incapable of interfering with relatively fast dynamic aeroelastic modes of behavior. The development of fast actuators and actuation mechanisms has allowed actuation to affect higher frequencies that correspond to "fast" aeroelastic motions instead of just rigid-body motions. This means that active controls may unintentionally excite modes and lead to undesirable dynamic aeroservoelastic behavior. At the same time, the availability of fast actuators has made AFS, and the synthesis of control laws to stabilize higher-frequency modes of behavior of the elastic vehicle possible.

Because of potential dangerous aeroservoelastic interactions and because AFS system failure can result in catastrophic events, one of the largest challenges that the application of AFS technology faces is certification, which means: safety and reliability. Active control systems certified on aircraft today (such as maneuver load control and gust load alleviation) meet redundancy and reliability requirements with demonstrated probability that is acceptable for aircraft safety. Such certification requirements are more difficult in the case of AFS due to the catastrophic nature of flutter. For example, if divergent flutter were involved, failure of any part of the AFS, unless enough

redundancy in the system guarantees compensation for such failure, may result in airframe failure that occurs too quickly for corrective action to be taken by a flight crew. AFS systems may seem currently as most acceptable if they suppress self-sustained aeroelastic behaviors of the very mild instability nature or limit-cycle oscillations (LCOs) with amplitudes of acceptable magnitude. the challenges that AFS technology maturation faces motivate more research and development in this area . For a thorough recent review of the field of AFS, see [1].

1.4 Needs and Contributions

The importance of testing, in the wind tunnel and in flight, of aeroservoelastic systems cannot be overstated. Even though miniaturization of actuators, sensors, and computing equipment has made the construction and flight tests of research unmanned aerial vehicles (UAVs) more practical than ever before, wind tunnel tests are still extremely valuable because of the possibility of tightly controlling test conditions and accurately measuring test results, and because, in the case of small wind tunnel models in small research wind tunnels, of the low cost and low risks involved. Wind-tunnel model and test information and results made available to the technical community would be valuable in contributing to the research required to develop design and analysis methods for AFS and for active control flight control in general.

Also beneficial would be a widely accepted formulation of the aeroservoelastic equations of motion (EOM), establishing consistency in "plant" modeling for active control synthesis. Such EOMs should be general and allow integration with industry standard modeling tools.

Comprehensive aeroelastic/aeroservoelastic reliability/uncertainty analysis methods and capabilities are also important to the safety and performance of such systems. Beyond guaranteeing safety, such methods deepen the understanding of the performance and multidisciplinary interactions of the complex aeroservoelastic systems involved. They can also help guide the establishment of required safety margins.

Finally, a great deal of effort still needs to be made in the area of control law design and imple-

mentation. This effort needs to focus on overcoming the challenges associated with safe operation of AFS systems, such as control of multiple flutter mechanisms, robustness in the face of uncertainty, avoidance of undesirable aeroservoelastic interactions, reliability, and costs.

This work will contribute to the state of the art in aeroservoelastic modeling for control synthesis by developing simulations for the frequency responses of a flexible wind tunnel model, designed, built, and tested at the University of Washington, and by comparing simulation results to experimental data. The wind tunnel model is described in Chapter 4. References [2] and [3] describe the work done by the University of Washington's team to date.

The simulations developed accept any control surface as the input and have any sensor measurement as the output. For purposes of this work, the focus is on an input from the elevator of the wind tunnel model to an accelerometer located at the wing tip of the wind tunnel model. The simulations developed generate frequency response functions based on structural and unsteady aerodynamic data extracted from a NASTRAN finite element model and on user-defined inputs. By developing such simulations for an aeroservoelastic model that can be compared against wind tunnel experimental data, this work contributes to addressing the need for increased confidence in analysis and design capabilities required for AFS development. Using the industry's widely used NASTRAN for generating structural and aerodynamic data the work presented here can be applied to any aeroservoelastic wind tunnel model or any actively controlled airplane in flight.

One of the mathematical formulations used here leads to an aeroservoelastic state-space representation. Since modern control law synthesis is widely based on this type of representation, the formulations developed and tested here create the foundation of aeroservoelastic plant modeling for modern AFS control law synthesis.

Chapter 2

MATHEMATICAL MODELING OF FREQUENCY RESPONSE METHODS

Two different analysis methods are developed and compared for finding the frequency response for various control surfaces as inputs to any particular sensor as an output. A list of common variables used throughout these derivations are described in Table 2.1.

Table 2.1: Equation variable descriptions.

Variable	Description
ω	Frequency (radians per sec)
$[M]$	Generalized mass matrix
$[K]$	Generalized stiffness matrix
q_D	Dynamic pressure
$[A]$	Generalized unsteady aerodynamic matrix
j	Imaginary unit
k	Reduced frequency
$\{q\}$	Generalized displacements vector
s (subscript)	Structural DOF
c (subscript)	Control motion DOF

2.1 Second-order Method

To begin, the Fourier-transformed equation of motion is written as follows:

$$\left[-\omega^2[M_{ss}] + [K_{ss}] - q_D[A_{ss}(jk)]\right]\{q_s\} + \Big[-\omega^2[M_{sc}] + [K_{sc}] - q_D[A_{sc}(jk)]\Big]\{q_c\} = \{0\} \tag{2.1}$$

For control surfaces that are free to rotate about their hinges, except for the torque provided by actuators: $[K_{sc}] = [0]$. For the particular system tested in this work (see later sections about its design and construction) we also assume that $[M_{sc}] = [0]$, although the simulation capabilities presented here can easily accept any $[M_{sc}]$. transfer functions simulated and measured in this work use unit control surface input amplitudes of 1°, and therefore, in the case of one control surface, $q_c = 1$. This simplifies the equation of motion for the case studied here to

$$\left[-\omega^2[M_{ss}] + [K_{ss}] - q_D[A_{ss}(jk)]\right]\{q_s\} = q_D A_{sc}(jk) \tag{2.2}$$

From equation (2.2), the generalized displacements, $\{q_s\}$, can be found.

$$\{q_s\} = \left[-\omega^2[M_{ss}] + [K_{ss}] - q_D[A_{ss}(jk)]\right]^{-1} q_D A_{sc}(jk) \tag{2.3}$$

The displacement in any out of plane z-degree of freedom, z_{acc} at the point where an accelerometer is installed can be determined for any frequency.

$$z_{acc}(\omega) = \{c\}^T\{q_s\} \tag{2.4}$$

where $\{c\}$ is a vector made up of the contributions, by superposition, of mode shapes, ϕ, to the z-dof motion at the point where the accelerometer is located.

$$\{c\} = \begin{Bmatrix} \phi_{11} \\ \phi_{21} \\ \vdots \\ \phi_{n1} \end{Bmatrix} \tag{2.5}$$

And so, the acceleration, a_{acc}, can be calculated at each frequency using the vertical displacement.

$$a_{acc}(\omega) = -\omega^2 z_{acc} \tag{2.6}$$

To account for structural damping in the system, a diagonal matrix, $[G]$, of structural damping coefficients, g_{st}, is multiplied by the generalized stiffness matrix of the system and added to the equation.

$$\left[-\omega^2[M_{ss}] + [G][K_{ss}] - q_D[A_{ss}(jk)]\right]\{q_s\} = q_D[A_{sc}(jk)]\{q_c\} \tag{2.7}$$

where

$$[G] = \begin{bmatrix} 1+jg_{st_1} & 0 & \dots & 0 \\ 0 & 1+jg_{st_2} & \dots & 0 \\ 0 & \vdots & \ddots & 0 \\ 0 & 0 & \dots & 1+jg_{st_n} \end{bmatrix} \tag{2.8}$$

So, equation (2.3) becomes

$$\{q_s\} = \left[-\omega^2[M_{ss}] + [G][K_{ss}] - q_D[A_{ss}(jk)]\right]^{-1} q_D A_{sc}(jk) \tag{2.9}$$

And again, equations (2.4-2.6) can be used to find the acceleration at location of interest. To integrate the actuators into this second-order method, the transfer function of the actuator is multiplied by that from the frequency response of the actuator to accelerator. The sensors are added in the same manner. The accelerometer transfer function is also multiplied by that from the frequency response with the actuator integration.

2.2 First-order Method

For the development of a standard linear time invariant (LTI) state space model of the aeroservoelastic system a Rational Function Approximation (RFA) (specifically, the Roger approximation) of the aerodynamic matrix must be found.

2.2.1 Roger Approximation

The Roger approximation is used to create a Laplace transform of the aerodynamic matrix, extending unsteady aerodynamic terms that are available for simple harmonic motions to the Laplace domain near the imaginary axis. We begin with a Fourier transform of the $[A(j\omega)]$ matrix which uses real $[P]$ matrices and real aerodynamic lag roots, β_n, for a series of aerodynamic lag terms.

$$[A(j\omega)] = [P_0] + j\omega[P_1] - \omega^2[P_2] + \frac{j\omega}{j\omega+\beta_1}[P_3] + \frac{j\omega}{j\omega+\beta_2}[P_4] + \dots \tag{2.10}$$

Using the relationship between frequency and reduced frequency,

$$j\omega = jk\frac{U}{b} \tag{2.11}$$

where U is the airspeed and b is the semi-chord, the approximation of the aerodynamic matrix can be described as

$$[A(jk)] \approx [P_0] + jk\frac{U}{b}[P_1] - k^2\left(\frac{U}{b}\right)^2[P_2] + \frac{jk}{jk+\frac{b}{U}\beta_1}[P_3] + \frac{jk}{jk+\frac{b}{U}\beta_2}[P_4] + \dots \tag{2.12}$$

This can be redefined as

$$[A(jk)] \approx [\bar{P}_0] + jk[\bar{P}_1] - k^2[\bar{P}_2] + \frac{jk}{jk+\bar{\beta}_1}[\bar{P}_3] + \frac{jk}{jk+\bar{\beta}_2}[\bar{P}_4] + \dots \tag{2.13}$$

where

$$[\bar{P}_0] = [P_0] \tag{2.14}$$

$$[\bar{P}_1] = [P_1]\frac{U}{b} \tag{2.15}$$

$$[\bar{P}_2] = [P_2]\left(\frac{U}{b}\right)^2 \tag{2.16}$$

$$[\bar{P}_3] = [P_3] \tag{2.17}$$

$$[\bar{P}_4] = [P_4] \tag{2.18}$$

$$\vdots \tag{2.19}$$

$$\bar{\beta}_1 = \beta_1\frac{b}{U} \tag{2.20}$$

$$\bar{\beta}_2 = \beta_2\frac{b}{U} \tag{2.21}$$

$$\vdots \tag{2.22}$$

By using a least squares approximation, the $[\bar{P}_n]$ matrices can be evaluated term by term, fitting the rational function approximation to tabulated unsteady aerodynamic matrices given over a range of reduced frequencies. For the m, n term:

$$\begin{bmatrix} 0 & -k_1^2 & \frac{k_1^2}{k_1^2+\bar{\beta}_1}^2 & \frac{k_1^2}{k_1^2+\bar{\beta}_2^2} & \cdots \\ k_1 & 0 & \frac{k_1\bar{\beta}_1}{k_1^2+\bar{\beta}_1^2} & \frac{k_1\bar{\beta}_2}{k_1^2+\bar{\beta}_2^2} & \cdots \\ \vdots & \vdots & \vdots & \vdots & \ddots \\ 0 & -k_n^2 & \frac{k_n^2}{k_n^2+\bar{\beta}_1^2} & \frac{k_n^2}{k_n^2+\bar{\beta}_2^2} & \cdots \\ k_n & 0 & \frac{k_n\bar{\beta}_1}{k_n^2+\bar{\beta}_1^2} & \frac{k_n\bar{\beta}_2}{k_n^2+\bar{\beta}_2^2} & \cdots \end{bmatrix} \begin{Bmatrix} \bar{P}_{1_{m,n}} \\ \bar{P}_{2_{m,n}} \\ \bar{P}_{3_{m,n}} \\ \bar{P}_{4_{m,n}} \\ \vdots \end{Bmatrix} \approx \begin{Bmatrix} \text{Re}(A_{m,n}(jk_1) - A_{m,n}(k_0 = 0)) \\ \text{Im}(A_{m,n}(jk_1)) \\ \text{Re}(A_{m,n}(jk_n) - A_{m,n}(k_0 = 0)) \\ \text{Im}(A_{m,n}(jk_n)) \end{Bmatrix} \tag{2.23}$$

After the $[\bar{P}]$ matrices are determined, the $[P]$ matrices can be found and (based on analytic continuation from the $j\omega$ axis to the Laplace domain s) an approximation in the Laplace domain is described as follows:

$$[A(s)] = [P_0] + s[P_1] + s^2[P_2] + \frac{s}{s+\beta_1}[P_3] + \frac{s}{s+\beta_2}[P_4] + \ldots \tag{2.24}$$

where s is the Laplace variable.

2.2.2 State-Space Formulation

The aeroelastic equations of motion and the actuator dynamics must be integrated into a standard state-space representation, as shown below.

$$\dot{x} = Ax + Bu \tag{2.25}$$

$$y = Cx + Du \tag{2.26}$$

Aeroelastic Plant

For the state-space representation of the aeroelastic plant without actuator dynamics, the equations of motion, including structural dynamic and unsteady aerodynamic effects, have to be brought to standard state space form.

To begin, the equations of motion are written in a partitioned form for the structural generalized displacements and forced control surface motions.

$$\left[\begin{bmatrix}[M_{ss}] & [M_{sc}]\\ [M_{cs}] & [M_{cc}]\end{bmatrix} s^2 + \begin{bmatrix}[C_{ss}] & [C_{sc}]\\ [C_{cs}] & [C_{cc}]\end{bmatrix} s + \begin{bmatrix}[K_{ss}] & [K_{sc}]\\ [K_{cs}] & [K_{cc}]\end{bmatrix} - q_D \begin{bmatrix}[A_{ss}(s)] & [A_{sc}(s)]\\ [A_{cs}(s)] & [A_{cc}(s)]\end{bmatrix}\right] \begin{bmatrix}\{q_s\}\\ \{q_c\}\end{bmatrix} = 0 \tag{2.27}$$

The equations above use a structural viscous damping math model (the matrix $[C]$) and they do not include the effects of external forces on the system such as gust loads. Focusing on the structural DOF equation of motion yields the following equation for the case of a single control surface input:

$$\left[[M_{ss}]s^2 + [C_{ss}]s + [K_{ss}] - q_D[A_{ss}(s)]\right]\{q_s\} + \Big[[M_{sc}]s^2 + [C_{sc}]s + [K_{sc}] - q_D A_{sc}(s)\Big] q_c = 0. \tag{2.28}$$

We now use the Roger rational function approximation of the generalized aerodynamic matrices. The number of terms in this equation is determined by the number of aerodynamic lag terms, β_n.

$$[A(s)] = [P_0] + s[P_1] + s^2[P_2] + \frac{s}{s+\beta_1}[P_3] + \frac{s}{s+\beta_2}[P_4] + ... \tag{2.29}$$

This is then partitioned into structure-structure and structure-control DOFs.

$$[[A_{ss}(s)], [A_{sc}(s)]] = [[P_{0_{ss}}], [P_{0_{sc}}]] + s\,[[P_{1_{ss}}], [P_{1_{sc}}]] + s^2\,[[P_{2_{ss}}], [P_{2_{sc}}]] + \frac{s}{s+\beta_1}\,[[P_{3_{ss}}], [P_{3_{sc}}]] + \frac{s}{s+\beta_2}\,[[P_{4_{ss}}], [P_{4_{sc}}]] + ... \tag{2.30}$$

The aerodynamic effects from unsteady forces are then introduced into the structural EOM by substituting (2.30) into (2.28).

$$\left[[M_{ss}]s^2 + [C_{ss}]s + [K_{ss}] - q_D\left[[P_{0_{ss}}] + s[P_{1_{ss}}] + s^2[P_{2_{ss}}] + \frac{s}{s+\beta_1}[P_{3_{ss}}] + \frac{s}{s+\beta_2}[P_{4_{ss}}] + ...\right]\right]\{q_s\} + \left[[M_{sc}]s^2 + [C_{sc}]s + [K_{sc}] - q_D\left[[P_{0_{sc}}] + s[P_{1_{sc}}] + s^2[P_{2_{sc}}] + \frac{s}{s+\beta_1}[P_{3_{sc}}] + \frac{s}{s+\beta_2}[P_{4_{sc}}] + ...\right]\right]\{q_c\} = 0 \tag{2.31}$$

The equation above is for multiple control surface inputs. A single control surface input will require that the sc matrices on the right hand side will become sc vectors. Also recall that $[K_{sc}] = [0]$ and that in our case we use $[M_{sc}] = [0]$. Defining modified mass, damping, and stiffness matrices as follows

$$\bar{M}_{ss} = M_{ss} - q_D P_{2_{ss}} \tag{2.32}$$

$$\bar{C}_{ss} = C_{ss} - q_D P_{1_{ss}} \tag{2.33}$$

$$\bar{K}_{ss} = K_{ss} - q_D P_{0_{ss}} \tag{2.34}$$

$$\bar{M}_{sc} = M_{sc} - q_D P_{2_{sc}} \tag{2.35}$$

$$\bar{C}_{sc} = C_{sc} - q_D P_{1_{sc}} \tag{2.36}$$

$$\bar{K}_{sc} = K_{sc} - q_D P_{0_{sc}} \tag{2.37}$$

allows (2.31) to be written in a more compact form:

$$\begin{aligned}
&\left[[\bar{M}_{ss}]s^2 + [\bar{C}_{ss}]s + [\bar{K}_{ss}]\right]\{q_s\} - q_D\left[\frac{s}{s+\beta_1}[P_{3_{ss}}] + \frac{s}{s+\beta_2}[P_{4_{ss}}] + ...\right]\{q_s\} + ... \\
&\left[[\bar{M}_{sc}]s^2 + [\bar{C}_{sc}]s + [\bar{K}_{sc}]\right]\{q_c\} - q_D\left[\frac{s}{s+\beta_1}[P_{3_{sc}}] + \frac{s}{s+\beta_2}[P_{4_{sc}}] + ...\right]\{q_c\} + ... = \{0\}
\end{aligned} \tag{2.38}$$

Equation (2.38) can be rearranged to yield

$$\begin{aligned}
&[\bar{M}_{ss}]s^2\{q_s\} + [\bar{C}_{ss}]s\{q_s\} + [\bar{K}_{ss}]\{q_s\} - q_D\left[[P_{3_{ss}}],[P_{3_{sc}}]\right]\frac{s}{s+\beta_1}\left\{\begin{array}{c}\{q_s\}\\ \{q_c\}\end{array}\right\} - \\
&q_D\left[[P_{4_{ss}}],[P_{4_{sc}}]\right]\frac{s}{s+\beta_2}\left\{\begin{array}{c}\{q_s\}\\ \{q_c\}\end{array}\right\} - ... = -[\bar{M}_{sc}]s^2\{q_c\} - [\bar{C}_{sc}]s\{q_c\} - [\bar{K}_{sc}]\{q_c\}
\end{aligned} \tag{2.39}$$

The aerodynamic lag states are defined as

$$\{r_1\} = q_D\left[[P_{3_{ss}}],[P_{3_{sc}}]\right]\frac{s}{s+\beta_1}\left\{\begin{array}{c}\{q_s\}\\ \{q_c\}\end{array}\right\} \tag{2.40}$$

$$\{r_2\} = q_D\left[[P_{4_{ss}}],[P_{4_{sc}}]\right]\frac{s}{s+\beta_2}\left\{\begin{array}{c}\{q_s\}\\ \{q_c\}\end{array}\right\} \tag{2.41}$$

$$\vdots$$

and so,

$$s\{r_1\} = -\beta_1[I]\{r_1\} + q_D[P_{3_{ss}}]s\{q_s\} + q_D[P_{3_{sc}}]s\{q_c\} \tag{2.42}$$

$$s\{r_2\} = -\beta_2[I]\{r_2\} + q_D[P_{4_{ss}}]s\{q_s\} + q_D[P_{4_{sc}}]s\{q_c\} \tag{2.43}$$

$$\vdots$$

Therefore, (2.39) becomes

$$[\bar{M}_{ss}]s^2\{q_s\} + [\bar{C}_{ss}]s\{q_c\} + [\bar{K}_{ss}]\{q_s\} - \{r_1\} - \{r_2\} - ... = -\left[[\bar{K}_{sc}], [\bar{C}_{sc}], [\bar{M}_{sc}]\right] \left\{ \begin{array}{c} \{q_c\} \\ s\{q_c\} \\ s^2\{q_c\} \end{array} \right\} \tag{2.44}$$

The states are defined as

$$\{x_p\} = \left\{ \begin{array}{cccc} \{q_s\} & \{\dot{q}_s\} & \{r_1\} & \{r_2\} \quad ... \end{array} \right\}^T \tag{2.45}$$

so that the state-space formulation can be achieved.

$$s\{x_p\} = [A_p]\{x_p\} + [B_p]\{\bar{q}_c\} \tag{2.46}$$

where

$$\{\bar{q}_c\} = \left\{ \begin{array}{c} \{q_c\} \\ s\{q_c\} \\ s^2\{q_c\} \end{array} \right\} \tag{2.47}$$

and

$$[A_p] = \begin{bmatrix} 0 & [I] & 0 & 0 & ... \\ [\bar{M}_{ss}]^{-1}[\bar{K}_{ss}] & [\bar{M}_{ss}]^{-1}[\bar{C}_{ss}] & [\bar{M}_{ss}]^{-1} & [\bar{M}_{ss}]^{-1} & ... \\ 0 & q_D[P_{3_{ss}}] & -\beta_1[I] & 0 & ... \\ 0 & q_D[P_{4_{ss}}] & 0 & -\beta_2[I] & ... \\ \vdots & \vdots & \vdots & \vdots & \ddots \end{bmatrix} \tag{2.48}$$

$$[B_p] = \begin{bmatrix} 0 & 0 & 0 \\ [-\bar{M}_{ss}]^{-1}[\bar{K}_{sc}] & [-\bar{M}_{ss}]^{-1}[\bar{C}_{sc}] & [-\bar{M}_{ss}]^{-1}[\bar{M}_{sc}] \\ 0 & q_D[P_{3_{sc}}] & 0 \\ 0 & q_D[P_{4_{sc}}] & 0 \\ \vdots & \vdots & \vdots \end{bmatrix} \tag{2.49}$$

Integration of Actuators

With the state-space representation of the plant formulated, the effects of the actuators can be integrated to create the system state-space representation. First, the generalized control surface dynamics are derived and integrated into the plant dynamics to create a system state-space representation. In the case studied here low order actuator dynamic models of actuator / control surface systems are used based on bench tests. With the subscript a denoting actuator state space models:

$$s\{x_a\} = [A_a]\{x_a\} + [B_a]\{u_a\} \tag{2.50}$$

$$\{q_c\} = \{y_a\} = [C_a]\{x_a\} \tag{2.51}$$

A strictly proper transfer function and a single-input, single-output (SISO) system are assumed for each actuator. All actuator models are then assembled into a state space model of the "actuators block", with $\{u_a\}$ being the vector of input commands to the actuators. This provides the following matrices,

$$[A_a] = \begin{bmatrix} [A_{a_1}] & & & \\ & [A_{a_2}] & & \\ & & \ddots & \\ & & & [A_{a_n}] \end{bmatrix} \tag{2.52}$$

$$[B_a] = \begin{bmatrix} \{B_{a_1}\} & & & \\ & \{B_{a_2}\} & & \\ & & \ddots & \\ & & & \{B_{a_n}\} \end{bmatrix} \tag{2.53}$$

$$[C_a] = \begin{bmatrix} \{C_{a_1}\}^T & & & \\ & \{C_{a_2}\}^T & & \\ & & \ddots & \\ & & & \{C_{a_n}\}^T \end{bmatrix} \tag{2.54}$$

$$\{x_a\} = \begin{Bmatrix} \{x_{a_1}\} \\ \{x_{a_2}\} \\ \vdots \\ \{x_{a_n}\} \end{Bmatrix} \tag{2.55}$$

The first derivative of equation (2.51) is taken and (2.50) is substituted in.

$$s\{q_c\} = [C_a]s\{x_a\} = [C_a][A_a]\{x_a\} + [C_a][B_a]\{u_a\} \tag{2.56}$$

The derivative of equation (2.56) is taken and (2.50) is substituted in.

$$\begin{aligned} s^2\{q_c\} &= [C_a][A_a]s\{x_a\} + [C_a][B_a]s\{u_a\} \\ &= [C_a][A_a][A_a]\{x_a\} + [C_a][A_a][B_a]\{u_a\} + [C_a][B_a]s\{u_a\} \end{aligned} \tag{2.57}$$

Equations (2.51), (2.56), and (2.57) can be written in matrix form as

$$\begin{Bmatrix} \{q_c\} \\ s\{q_c\} \\ s^2\{q_c\} \end{Bmatrix} = \begin{bmatrix} [C_a] \\ [C_a][A_a] \\ [C_a][A_a][A_a] \end{bmatrix} \{x_a\} + \begin{bmatrix} 0 & 0 \\ [C_a][B_a] & 0 \\ [C_a][A_a][B_a] & [C_a][B_a] \end{bmatrix} \begin{Bmatrix} \{u_a\} \\ s\{u_a\} \end{Bmatrix} \tag{2.58}$$

Alternative vectors and matrices are defined

$$\begin{Bmatrix} \{q_c\} \\ s\{q_c\} \\ s^2\{q_c\} \end{Bmatrix} = \{\bar{q}_c\} \tag{2.59}$$

$$\begin{bmatrix} [C_a] \\ [C_a][A_a] \\ [C_a][A_a][A_a] \end{bmatrix} = [\bar{C}_a] \tag{2.60}$$

$$\begin{bmatrix} 0 & 0 \\ [C_a][B_a] & 0 \\ [C_a][A_a][B_a] & [C_a][B_a] \end{bmatrix} = \begin{bmatrix} [\bar{D}_{a_1}] & [\bar{D}_{a_2}] \end{bmatrix} = [\bar{D}_a] \tag{2.61}$$

such that (2.58) can be written as

$$\{\bar{q}_c\} = [\bar{C}_a]\{x_a\} + [\bar{D}_a] \left\{ \begin{array}{c} \{u_a\} \\ s\{u_a\} \end{array} \right\}. \tag{2.62}$$

Noting that $\{\bar{q}_c\} = \{\bar{y}_a\}$, it can be seen that (2.62) is the output equation state-space representation for the actuators. Equation (2.62) can be substituted into (2.46),

$$s\{x_p\} = [A_p]\{x_p\} + [B_p][\bar{C}_a]\{x_a\} + [B_p] \left[\begin{array}{cc} [\bar{D}_{a_1}] & [\bar{D}_{a_2}] \end{array} \right] \left\{ \begin{array}{c} \{u_a\} \\ s\{u_a\} \end{array} \right\} \tag{2.63}$$

Therefore, (2.50) and (2.63) can be combined in matrix form to achieve the state-space representation input equation with both plant and actuator dynamics.

$$s \left\{ \begin{array}{c} \{x_p\} \\ \{x_a\} \end{array} \right\} = \begin{bmatrix} [A_p] & [B_p][\bar{C}_a] \\ 0 & [A_a] \end{bmatrix} \left\{ \begin{array}{c} \{x_p\} \\ \{x_a\} \end{array} \right\} + \begin{bmatrix} [B_p][\bar{D}_{a_1}] & [B_p][\bar{D}_{a_2}] \\ [B_a] & 0 \end{bmatrix} \left\{ \begin{array}{c} \{u_a\} \\ s\{u_a\} \end{array} \right\} \tag{2.64}$$

When low order actuator dynamics are considered, the state-space representation defined by equation (2.64) are often simplified to include an actuator transfer function with a numerator that is lower than the denominator order by two or more. In this case,

$$[C_a][B_a] = [0]. \tag{2.65}$$

This modifies the matrix $[\bar{D}_a]$ such that

$$[\bar{D}_a] = \begin{bmatrix} 0 & 0 \\ 0 & 0 \\ [C_a][A_a][B_a] & 0 \end{bmatrix} = \left[\begin{array}{cc} [\bar{D}_{a_1}] & 0 \end{array} \right] \tag{2.66}$$

And so, (2.64) becomes

$$s \left\{ \begin{array}{c} \{x_p\} \\ \{x_a\} \end{array} \right\} = \begin{bmatrix} [A_p] & [B_p][\bar{C}_a] \\ 0 & [A_a] \end{bmatrix} \left\{ \begin{array}{c} \{x_p\} \\ \{x_a\} \end{array} \right\} + \begin{bmatrix} [B_p][\bar{D}_{a_1}] \\ [B_a] \end{bmatrix} \{u_a\}, \tag{2.67}$$

which can be written as

$$s\{x\} = [A_{sys}]\{x\} + [B_{sys}]\{u_a\}. \tag{2.68}$$

For integration of the sensors, the sensor transfer function, in this case the accelerometer, is converted to a state-space model and handled in the same way.

2.2.3 Frequency Response

Beginning with the state-space formulation developed so far, with multiple control surfaces

$$s\{x\} = [A_{sys}]\{x\} + [B_{sys}]\{u_a\} \tag{2.69}$$

we proceed to the case of one control surface input $u_a = 1$. The following equation can be used for the frequency response:

$$[j\omega[I] - A_{sys}]\{x\} = \{B_{sys}\} \tag{2.70}$$

Once the states, $\{x\}$ are found as functions of ω, they can be used to find velocities at structural points by multiplying by a vector, $\{\bar{c}\}$.

$$v(\omega) = \{\bar{c}\}^T\{x\} \tag{2.71}$$

The $\{\bar{c}\}$ vector is made of zeros for the states that correspond to the generalized displacements, lag states, and actuator states and includes the $\{c\}$ vector, which is made up of the contributions of mode shapes in the states corresponding to the generalized velocities.

$$\{\bar{c}\}^T = \left\{ \begin{array}{ccccc} \{0\} & \{c\}^T & \{0\} & \dots & \{0\} \end{array} \right\} \tag{2.72}$$

The acceleration can be described as the derivative of the velocity at each frequency.

$$a(\omega) = j\omega v(\omega) \tag{2.73}$$

Substituting equation (2.71) into (2.73) yields

$$a(\omega) = j\omega\{\bar{c}\}^T\{x\} = \{\bar{c}\}^T j\omega\{x\}. \tag{2.74}$$

A final equation for the acceleration using the state-space formulation can be found by substituting equation (2.69) into (2.74).

$$a(\omega) = \{\bar{c}\}^T[A_{sys}]\{x\} + \{\bar{c}\}^T[B_{sys}]\{u\} \tag{2.75}$$

Chapter 3

SIMULATION CAPABILITY

3.1 NASTRAN Model

The test case that will be used in for the frequency response function simulations is described in detail in Chapter 4. The finite element model (FEM) of this case was created in NASTRAN using a "ball-and-stick" method. This model consists of discrete concentrated masses and beam elements.

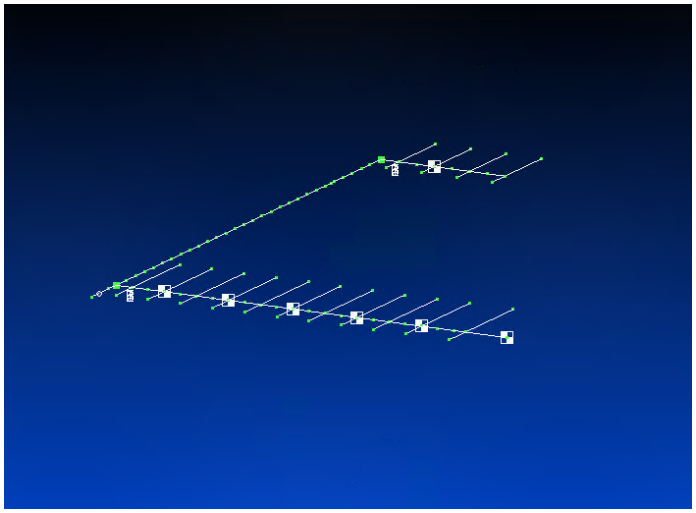

Figure 3.1: Structural elements of the finite element model.

For the aero-structural modeling of the test case, doublet lattice method (DLM) unsteady aerodynamic modeling was used along with NASTRAN splines between structural and aerodynamic meshes.

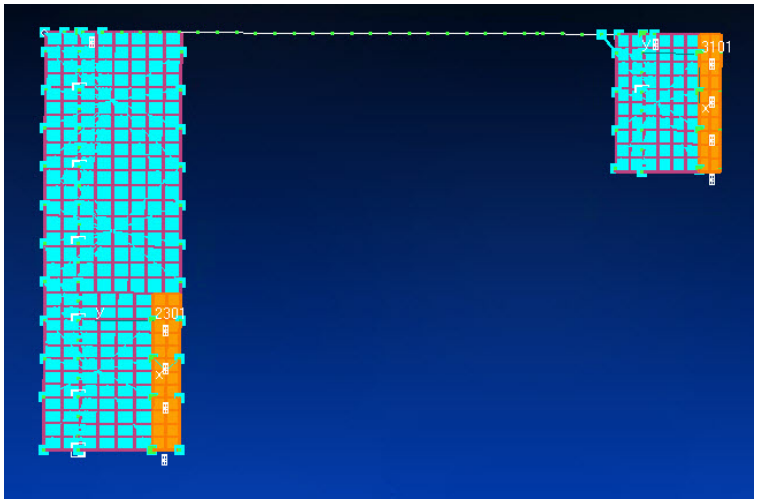

Figure 3.2: Aero-structural finite element model.

In order to create a MATLAB simulation of the frequency response functions of the test case, data from the FEM was extracted from NASTRAN to be used as inputs. This is especially important because it allows a way for unsteady aerodynamic methods to be taken from commercial codes and used for simulation. The matrices and values that were taken from the FEM for input into the MATLAB simulation are as follows:

- Matrix consisting of the grid points and associated x, y, and z coordinates
- Vector of the reduced frequencies, $\bar{k}$, used in FEM simulations
- Generalized mass and stiffness matrices, $[M_{HH}]$ and $[K_{HH}]$, respectively
- Unsteady aerodynamic matrices, $[Q_{HH}(jk)]$, for each reduced frequency (does not include dynamic pressure, q_D)
- Matrix containing the eigenvectors for each mode at all grid points, $[\phi]$

3.2 MATLAB Simulation

The goal of the MATLAB simulation is to take the inputs extracted from the NASTRAN model and find the frequency response of any actuator input to any sensor output. In the present study we focus on elevator input and accelerometer output at the wing tip. Other required inputs to the simulation are listed in Table 3.1.

Table 3.1: User-defined required simulation inputs.

Variable	Description
ρ	Density
b	Semi-chord (reference length)
ns	Number of structural modes
nc	Number of control modes
ζ	Damping ratio
β_n	Aerodynamic lag terms
U	Flight speed
U_{max}	Maximum speed for flutter prediction
TF_{act}	Actuator transfer function
pt	Grid point at which to evaluate frequency response

The simulation first finds the Roger approximation of the aerodynamic matrices and generates plots to compare the actual unsteady aerodynamic matrix values to those found via the approximation. The $[\bar{P}]$ approximation matrices are required for the flutter prediction using the root locus method which is evaluated next. Flutter predictions are also done using the U-g method. After these flutter predictions, the frequency response simulations are performed.

The second-order method generates a frequency response to be plotted, along with outputting

the required $\{c\}$ vectors for determining the displacement and acceleration at the wing tip. Next, the plant dynamics for the state-space formulation are developed and then the actuator dynamics are added using the transfer function of the actuator as defined by the user. After the low-order actuators are added, the first-order frequency response model is complete and state space frequency response simulations can be carried out. The frequency response results obtained by these two methods are then plotted together with the experimental data that is used for comparison. A flowchart of this process is shown in Appendix A.

Chapter 4

TEST CASE

The tests used for this study are based on the Model for Aeroelastic Response to Gust Excitation (MARGE) [2, 3]. This experimental system consists of three main components: the aeroelastic test article (MARGE), the gust generation system, and the wind tunnel. MARGE and the gust generation system are installed into the wind tunnel as shown in Figure 4.1. The experimental system was designed to be capable of testing various types of active control. The gust generation system is not required for the frequency response functions of an actuator input to sensor output and therefore will not be discussed here.

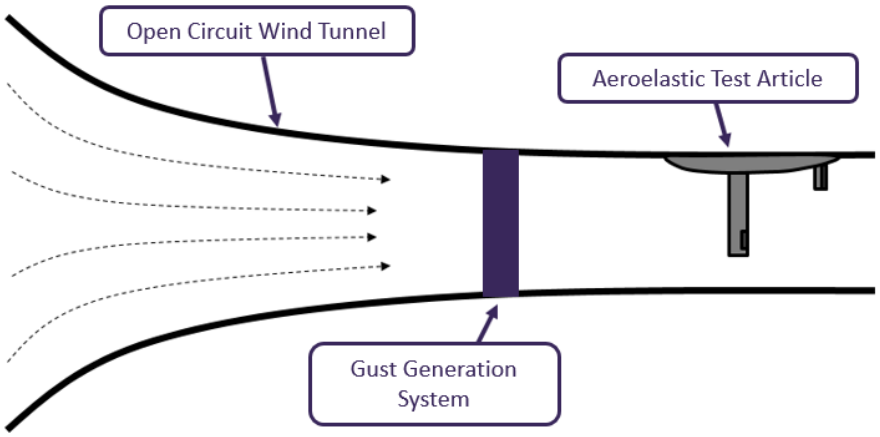

Figure 4.1: Wind tunnel testbed sideview.

The miniaturization of electronic and mechanical hardware in recent years and the low costs

involved have led other organizations to develop aeroservoelastic wind tunnel testing capabilities. References [4] - [12] describe a few of such efforts.

4.1 Test Article

Since the experimental system was designed for testing gust load alleviation, the test article was required to have aeroservoelastic dynamics conducive to this testing. This included frequency requirements of various modes that would be within the frequency band of low-cost actuators. This resulted in a very flexible model. Another important factor in the design of the test article was modularity. By designing a modular test article, the frequencies and aero-structural characteristics are easily changeable to accommodate requirements for any type of active control testing without the need for costly changes of any other aspects of the experimental system.

4.1.1 Structure

The test article uses a simple wing-fuselage-tail design. It simulates a half airplane design and hangs from a sub-assembly that is used for installation in the wind tunnel as shown in Figure 4.2. A ceramic bearing is located in the hanging sub-assembly to allow the test article to have a free rigid body pitch DOF. Each of the main components of the article use a beam to achieve the desired characteristics for the model. The wing and tail beams have 3-D printed aerodynamic shells that help define an aerodynamic shape of the test article while still allowing the beam to determine the model's stiffness characteristics. All of the aero shells use a NACA 0012 airfoil cross-section. There are foam fillers between the aero-shells that make up the wing to help maintain the desired aerodynamic shape while not affecting the stiffness of the structure.

The beam and shell design contributes to the modularity of the article since the beams can be replaced if different characteristics are desired and the shells can be added or taken away if necessary. Active shells include an internal actuation system and a control surface, while the passive shells are simply for aerodynamic passive shaping. Using 3-D printed shells also benefits

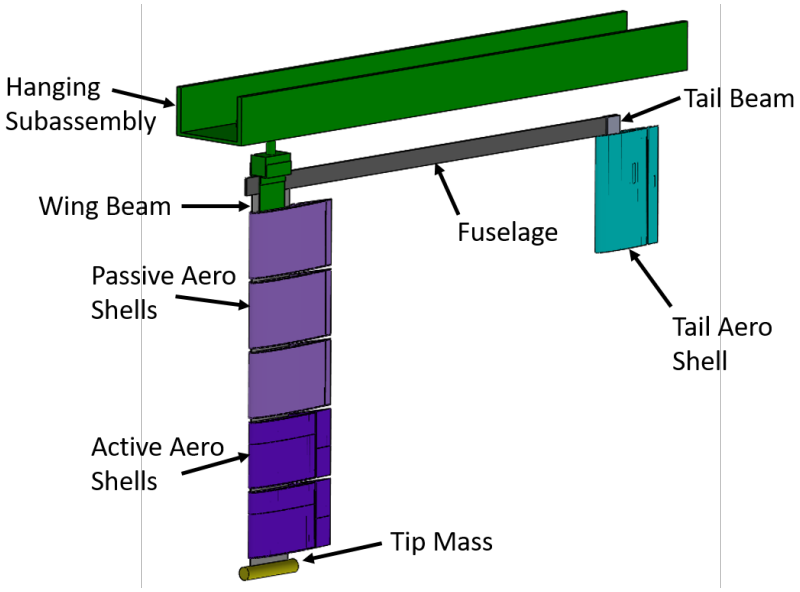

Figure 4.2: Overall test article assembly.

the modularity since they can be very quickly modified and manufactured while maintaining the same attachment system to the wing beam. The control surface(s) can be modified by changing the number and location of active shells. In addition to the beam and shells, the wing includes a tip mass (with its cg location and moment of inertia) that can be changed to help achieve the desired characteristics.

For this specific test case, the aero-structural requirements included frequencies as outlined in Table 4.1. In order to achieve these characteristics, the structural components were determined as listed in Table 4.2.

4.1.2 Actuation

The test article required two actuators for the active shells in the wing and one actuator for the tail. When determining the actuation that would be used, physical limitations and cost were considered. Hobby servo motors proved to be a sufficient option for the test article since they could nest inside

Table 4.1: Desired aero-structural characteristics for test case.

Mode	Frequency Requirement
Short-period	$<$1 Hz
First wing bending	Within 1 Hz of short-period
First wing torsion	$>$10 Hz
First fuselage bending	$>$7 Hz

of the aero-shells and they are inexpensive. The challenge presented with hobby servos, however, was that the bandwidth was not specified by the manufacturers. It was important to choose actuators that had a bandwidth that would encompass the frequencies of key modes. For the tests described here, the rigid body short period and the first bending frequency of the wing were important. To ensure that this would be the case, the servos were tested to find their actual bandwidth and to identify a valid transfer function estimate.

The servo motor chosen for this test case was the MKS HV6130. The specifics of this motor are described in Table 4.3.

To identify the important requirement of bandwidth as well as find a transfer function estimate of the actuator, a system identification test was done on the servo in which a sinusoidal input was varied linearly in frequency from 0.1 Hz to 10 Hz over a sixty second duration with a commanded amplitude of 15°. A potentiometer was used to measure the position of the servo. The time history and coherence estimate are shown in Figure 4.3.

From the testing, the bandwidth of the actuator was found to be approximately 4.5 Hz. Using a second-order system, two transfer functions were estimated. Figure 4.4 shows the frequency response function that was used to determine the bandwidth as well as the two transfer function estimates.

Table 4.2: Overview of structural components.

(a) Materials

Component	Material
Wing Beam	Aluminum 6061-T6
Tip Cyliner	Brass
Aero-shell	Polylactic Acid (PLA)
Fuslage Beam	Low Carbon Steel
Tail Beam	Aluminum 6061-T6

(b) Masses

Component	Weight (lb)
Wing Beam	0.367
Tip Cylinder	0.276
Active Aero-shell	0.209
Passive Aero-shell	0.132
Fuselage Beam	0.986
Tail Beam	0.146

For this case, the low-order transfer function (without a zero) shown in equation (4.1) will be used, which has a fit of 90.9% as reported by the transfer function estimate routine.

$$\hat{G}_(s) = \frac{1394}{s^2 + 62.2s + 1461} \tag{4.1}$$

4.1.3 Sensing

To accurately capture the response of the test article to the gust generation system and for control purposes, a variety of sensors were necessary. First, the position in the pitch DOF was captured by a Hall effect sensor (HES). The HES is a non-contact sensor that includes two components: a magnet and a stationary sensor. The sensor portion remains on the static mounting fixture, while the magnet is placed on the rod that the test article is suspended from. The sensor voltage output varies in response to the the rotation of the magnet due to the change in relative orientation of the two components.

There is a pair of uni-directional accelerometers located on the end of the wing beam in the

Table 4.3: MKS HV6130 wing servo specified characteristics.

Property	Value
Torque	$8.1\ kg - cm$
Speed	$0.1\ s$
Working Frequency	$1520\mu s\ /333\ Hz$

fore and aft corners. The accelerometers are used to measure the wing low-frequency bending and torsion. In addition to these sensors on the wing, there is a strain gauge located at the wing root to measure bending load. There is also a strain gauge on the fuselage to again measure bending load.

Lastly for sensing, there are rotary potentiometers on the output shafts of each of the servo motors. These potentiometers not only help from a control perspective, but they also aid in monitoring the servo motors since the motors are subject to gear slippage, overheating, and variable performance with variation in input voltage.

4.2 Wind Tunnel

4.2.1 Tunnel Description

Of the two wind tunnels at the University of Washington, the smaller wind tunnel was chosen for the experiments due to its availability and low cost. It has a closed $3' \times 3'$ test section and is an open return tunnel with an aft turbine. There are locations for top or bottom mounting. The tunnel has a testing speed ranging from 10 to 40 psf.

4.2.2 Test Article Installation

Due to the flexibility of the test article, it was decided that the top mounting in the test section would be the best option. For testing purposes, since responses to gust inputs were of major interest, it was

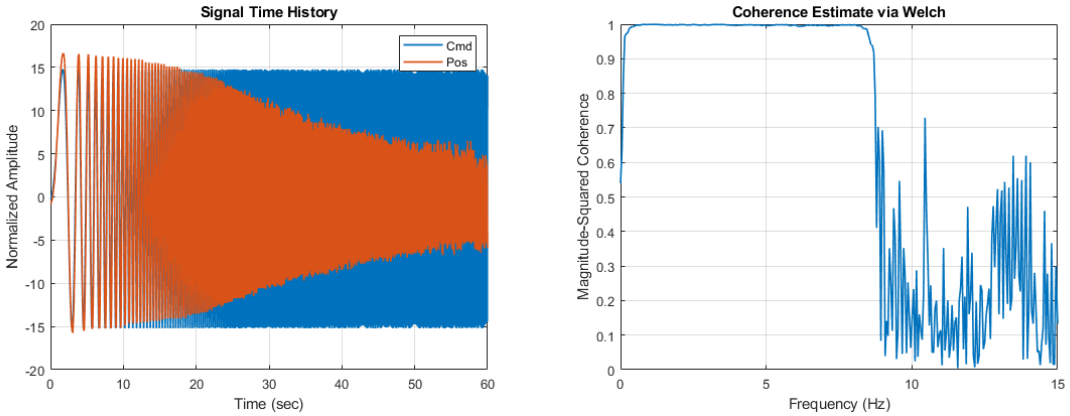

(a) Input-output time histories.

(b) Mean-squared signal coherence.

Figure 4.3: Signals used for servo system identification.

important to be ensured that the test article would see a gust with the desired amplitude. With the final design of gust generation vanes (to be discussed in future publications) first estimates of the gust intensity can be seen for the length of the tunnel in Figure 4.5, compared with measurements of gust angles due to a system of gust vanes in a much larger tunnel at the Polytechnic of Milan. The estimates presented in the figure are preliminary but, as can be seen in the figure, there is great variance in the gust amplitude along the length of the test section close to the gust vanes, and gust amplitudes decay quickly away from the vanes.

Therefore, an important factor for installation of the test article into the tunnel was the distance of the test article from the vanes. To maintain the modularity of the test article in this regard, the hanging sub-assembly was designed to allow the test article to be moved as desired in the direction of flow in the test section. The sub-assembly consists of an aluminum U-channel that contains various components, such as the HES and printed circuit board (PCB), required for the operation of the test article. The sub-assembly hangs from the top of the tunnel by use of a clamping system which allows for easy maneuvering of the position of the test article and hanging sub-assembly.

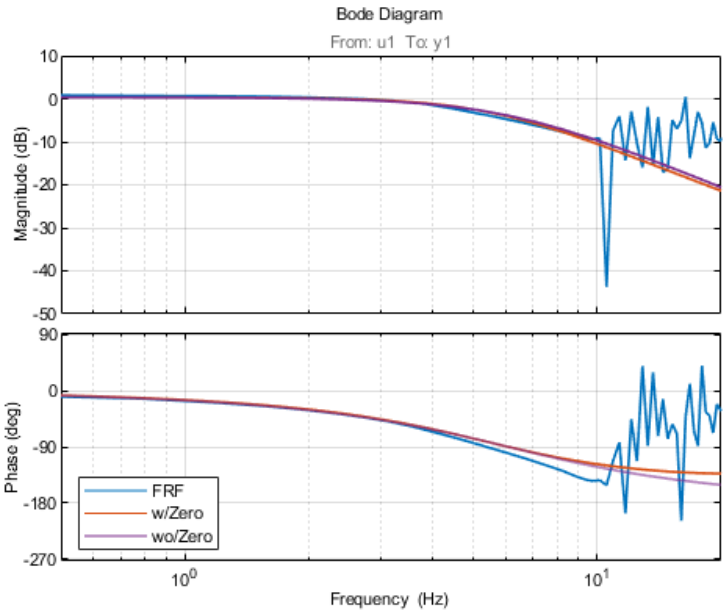

Figure 4.4: Estimated frequency response function and candidate transfer functions.

The implementation of this system is depicted in Figure 4.6.

4.3 Test Techniques

4.3.1 Ground Vibration Testing

Details of the ground testing work done on the system are described here to make the thesis self-contained, but they can also be found in references [2, 3, 13]. Prior to the start of wind tunnel testing, a series of tests were completed on the model to verify different aspects of the test article characteristics. In addition to the servo identification test, laser vibrometer tests were completed to evaluate the structural dynamics of the test article. Because the test article is comprised of beams and aerodynamic shells, where the beams are meant to capture the desired structural properties, tests needed to be done to ensure that the aerodynamic shells did not add an unexpected amount

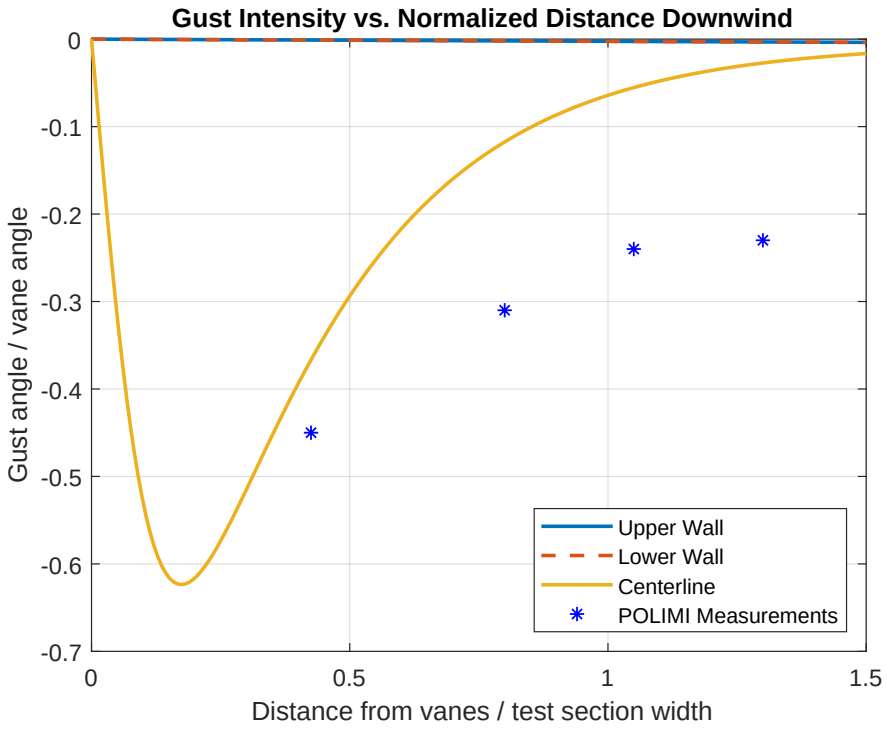

Figure 4.5: Result of preliminary two-dimensional steady gust vane effect analysis.

of stiffness to the test article. The first natural frequency of the beam with and without shells was determined analytically and compared to experimental data from the laser vibrometer tests. From the experimental data, it was found that the frequency in the case of the beam with aerodynamic shells was lower than the predicted frequency for that case by a measure captured by analysis where the aero-shells were modeled as added masses. Therefore, it was concluded that the shells do not have a substantial impact on the effective stiffness of the wing.

4.3.2 First Wing Bending

The first wing bending mode's frequency was determined both analytically and experimentally to be approximately 1.4 Hz, which is within the bandwidth of the servos. This allows the mode to be

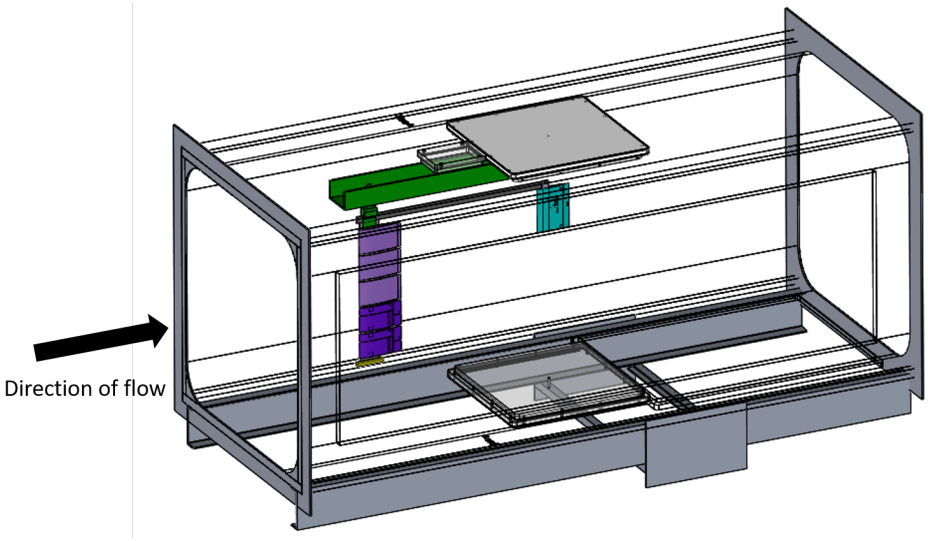

Figure 4.6: Configuration of the test article and mounting equipment in the context of the wind tunnel test section.

identifiable with sine-swept actuator inputs.

The damping ratio for the first wing bending mode was also determined. To find the value of the damping ratio, ζ, laser vibrometer testing was done. The response of the structure was measured via a laser vibrometer after the structure was excited by an instrumented impact hammer. Using the log-decrement method, the damping ratio of the first wing bending was calculated. Figure 4.7 shows varying calculated values for the damping ratio based on the presence of a tip mass and foam inserts between the aerodynamic shells. It can be seen that there is a variation of the damping ratio in the range of $\zeta \approx 0.004$ to 0.02.

Testing was also completed in the wind tunnel to verify this value and the damping ratio was found to actually be greater. This was determined via a dwell test near the expected first wing bending frequency. The input signal was commanded to an actuator and then abruptly stopped. The exponential decay was then measured at the wing tip using the laser vibrometer. This test was completed with each actuator as the input and similar results were achieved among these tests. The

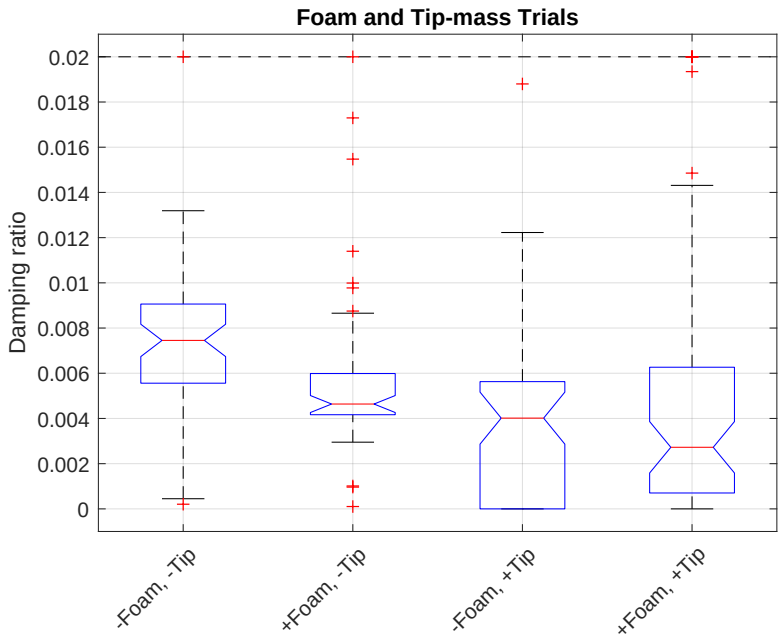

Figure 4.7: Changes in first wing bending damping due to foam and tip mass.

input command and the laser displacement of the test with the inboard aileron as the commanded actuator as shown in Figure 4.8.

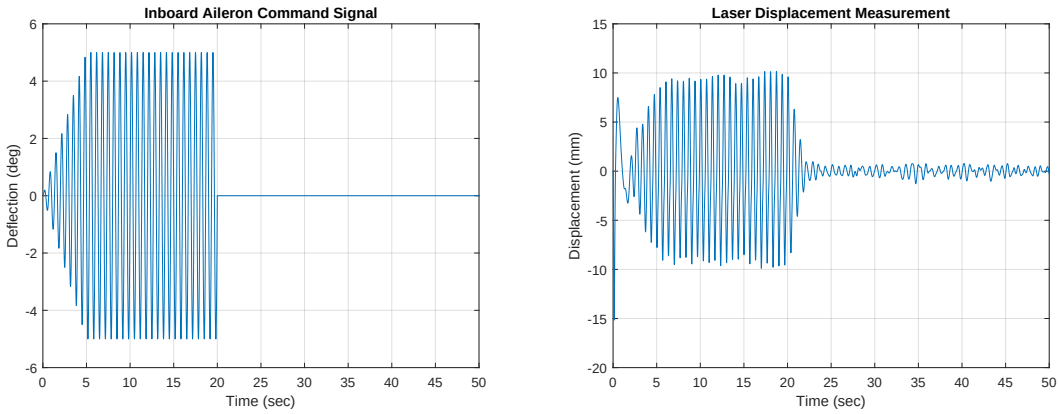

(a) Aileron dwell input signal

(b) Laser measurement of wing displacement

Figure 4.8: Time histories of input and measurement signals used in dwell tests for identification of first wing bending damping ratio.

4.3.3 Frequency Sweeps

Although many tests were performed in the wind tunnel, the tests of interest for comparison to the frequency response simulations are the control surface frequency sweeps. Tests were 6done for the inboard aileron, outboard aileron, and elevator as inputs for the sweep. However, this work will primarily focus on the elevator sweeps. At 60% of the target dynamic pressure, or 20.8 m/s, the elevator rotation was swept on from [0.01-1] Hz for over 100 seconds. This was then repeated for frequencies of [0.01-2] Hz. The amplitude of the sweeps were ramped-up over the first 10 seconds and then ramped-down to 50% over the last 15 seconds. The maximum amplitude for the elevator for these tests was 5°. The frequency responses of elevator input to wing tip acceleration were evaluated and are used as the experimental case for comparison to the simulations.

Chapter 5

ANALYTICAL PREDICTIONS

5.1 Roger Approximation

The Roger approximation of the unsteady aerodynamic matrices was compared against the actual tabulated values over the range of reduced frequencies used to validate the use of the Roger approximation in the first-order state space frequency response method. The Roger rational function approximation uses the $[\bar{P}]$ matrices and the form of Equation (2.13). Figure 5.1 shows a comparison of the first row of elements of the approximation and the actual values for both the real and imaginary parts of each element. As the figures show, the Roger approximation agrees very well with the actual aerodynamic matrix.

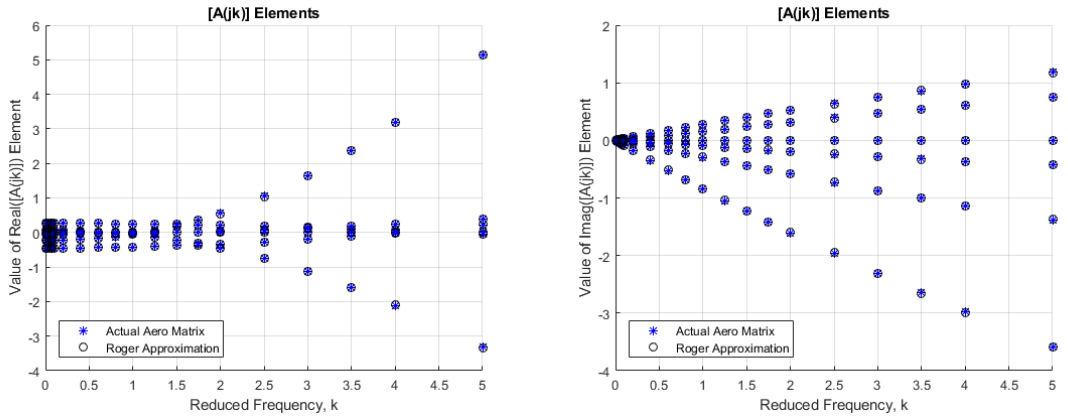

(a) Real elements.

(b) Imaginary elements.

Figure 5.1: Comparison of Roger approximation values to actual values

5.2 Flutter Prediction

Two methods in the new simulation were used to predict the flutter speed of the test article: the U-g method and the Root Locus method. The methods are described in Appendix B. A comparison of the predicted values from each method for the flutter speed and frequency are shown in Table 5.1. These predictions were verified by comparing to the results from NASTRAN simulations, which are based on the p-k method. The error between the two methods to the NASTRAN prediction for the flutter speed is -0.35% for the U-g method and -0.25% for the Root Locus method. The predicted frequencies for these methods also had very small errors relative to the NASTRAN value at approximately 0% and 0.24%, respectively. The low error in flutter prediction for both methods not only verifies the Roger approximation, but also validates the lag terms that were used in the Roger Approximation.

Table 5.1: Flutter prediction values.

Method	Predicted Speed (m/s)	Predicted Frequency (Hz)
Ug	201.3	4.20
Root locus	201.5	4.21
NASTRAN	202.0	4.20

5.2.1 U-g Method

The U-g method finds the artificial structural damping of the system at each flight speed that would be required to bring the system to simple harmonic motion. The flutter speed occurs where the artificial structural damping becomes greater than zero and is associated with a specific frequency. The plots for the artificial structural damping vs. flight speed and the frequency vs. flight speed for the case studied here are shown in Figure 5.2.

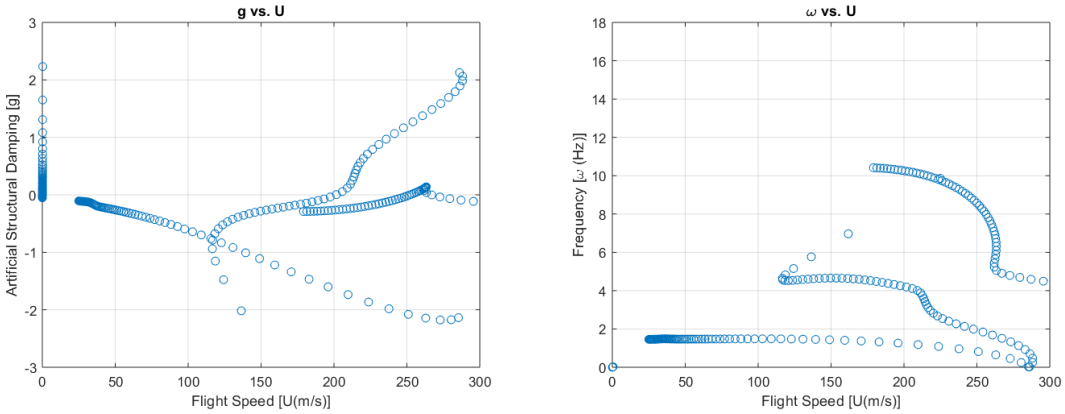

(a) Artificial structural damping result.

(b) Frequency result.

Figure 5.2: Ug method flutter analysis.

5.2.2 Root Locus Method

The Root Locus method uses the eigenvalues of the state space aeroelastic plant matrix to determine the flutter speed. The imaginary part of the eigenvalues are plotted against the real part. The flutter speed and frequency correspond to the eigenvalue that crosses the real axis. The plot of these eigenvalues is shown in Figure 5.3.

5.3 Initial Frequency Response Results

The frequency responses shown here are initial results that include no fine-tuning based on physical effects or comparisons, as those are discussed in 6. The simulation obtained by the second-order method is shown in Figure 5.4. It can be seen that the first wing bending peak occurs at 1.4 Hz, which agrees with what was measured in the testing.

The result of the first-order method is seen in Figure 5.5. Again, it can be seen that the first wing bending peak occurs at 1.4 Hz. Note that in both cases, a short period frequency occurs at about 1 Hz. So, there is some level of confidence in the performance of the simulation codes prior

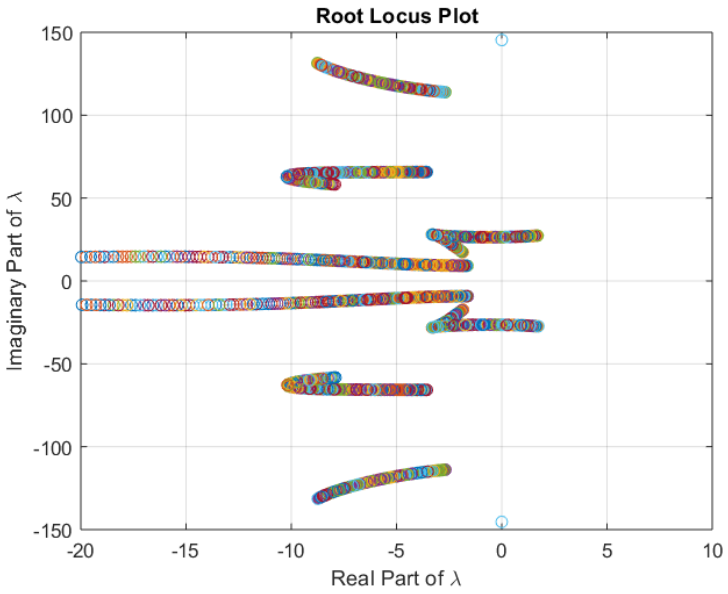

Figure 5.3: Result of root locus flutter analysis.

to comparing to experimental data since the frequencies are as expected from prior analytical and experimental predictions.

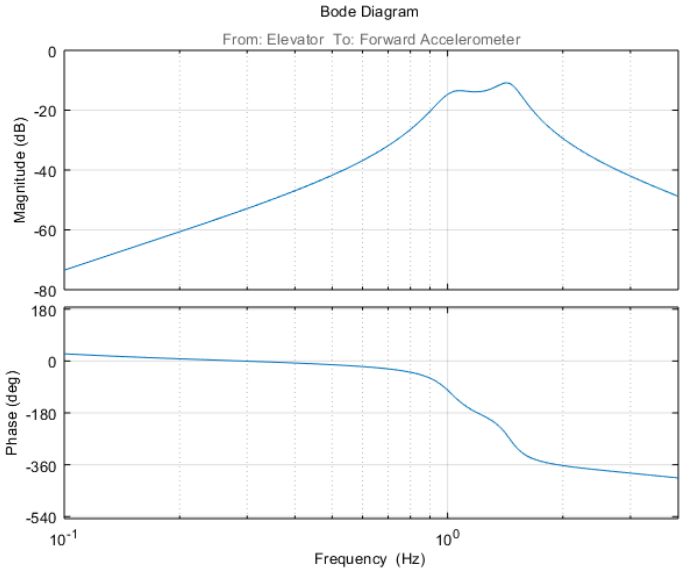

Figure 5.4: Second-order method results.

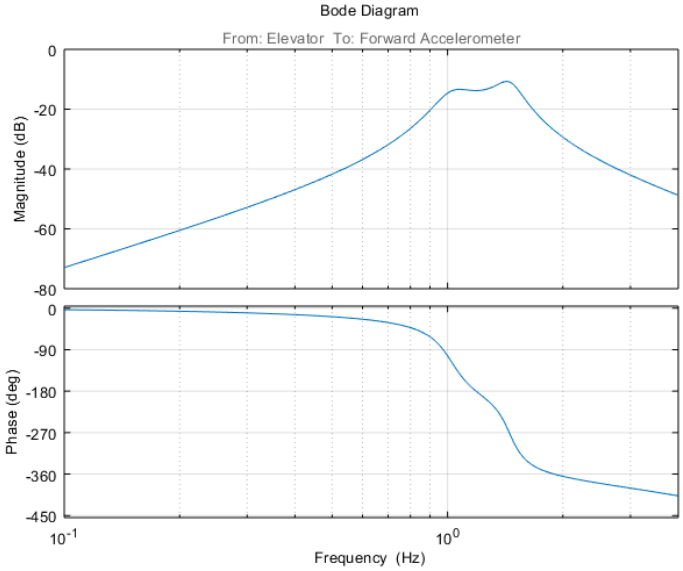

Figure 5.5: First-order method results.

Chapter 6

TECHNICAL DISCUSSION

6.1 Initial Comparisons

6.1.1 Between Methods

A comparison between the second order and first order state space methods to verify that they are indeed getting similar result has already been presented. See: Figure 6.1.

6.1.2 To Experimental Data

Next, the simulations from both methods are compared to the experimental data measured by the frequency sweeps. These results are shown in Figure 6.2.

From a first look at this data, it is evident that there is a large portion prior to, as well as after, the peak of first wing bending where the experimental data varies greatly from the simulated results. However, the range of importance for these results is from about 0.9 Hz to 2.5 Hz. Outside of this range, there is poor coherence for the experimental data, due to poor performance of the accelerator at low frequency and poor performance of the elevator actuator at high frequencies, and so the comparison of simulation to data in those regions cannot be trusted.

When examining the area of importance, it is noted that the simulation curve fits the trend very well to the experimental data. However, the magnitude of the simulation is slightly higher than the experimental data. The magnitude difference was analyzed, and it was determined that multiple factors contributed to the variance, which are discussed in later sections.

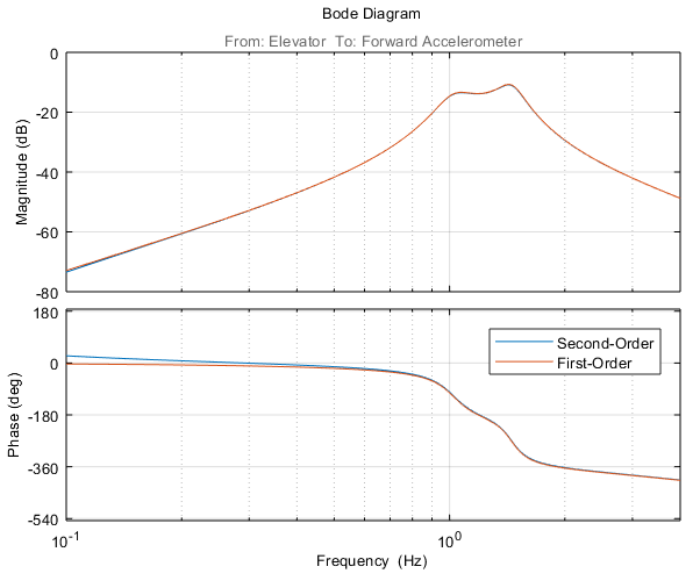

Figure 6.1: Comparison of both methods.

6.2 Fine-tuning of the Simulation Codes

6.2.1 $\{A_{sc}\}$ Correction Effects

Due to the non-linearity of control surface effectiveness, a correction factor must be applied to the structural-control portion of the aerodynamic matrix. The DLM method used in the aerodynamic analysis in NASTRAN assumes attached flow. However, in reality, the flow can separate over parts of the elevator and so the actual forces due to deflection of the elevator are smaller than the predictions from the DLM. Therefore, a correction factor multiplies the $\{A_{sc}\}$ column associated with the elevator.

Typical correction factors for small full-span control surfaces range from 0.4 to 0.6. As can be seen in Figure 6.3, the simulations fit the test data best (especially the peak response) in the range of frequency of good test result coherence if a correction factor of 0.4 is used.

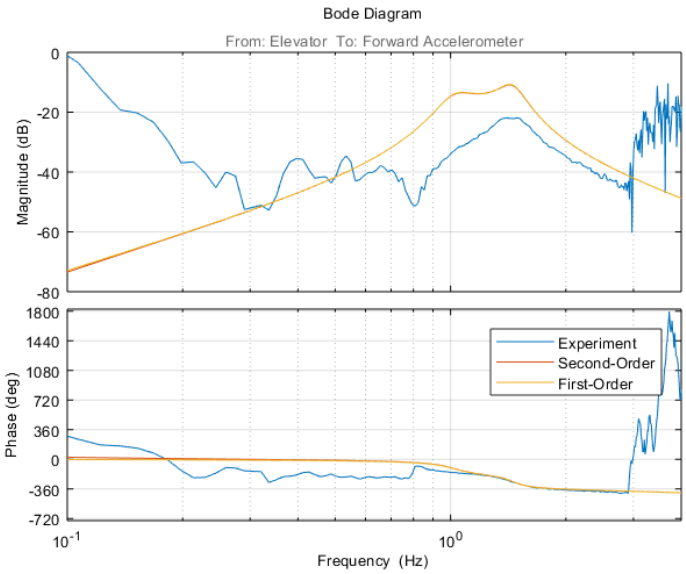

Figure 6.2: Comparison of simulations to experimental data before accounting for damping, aerodynamic efficiency, and root gap effects.

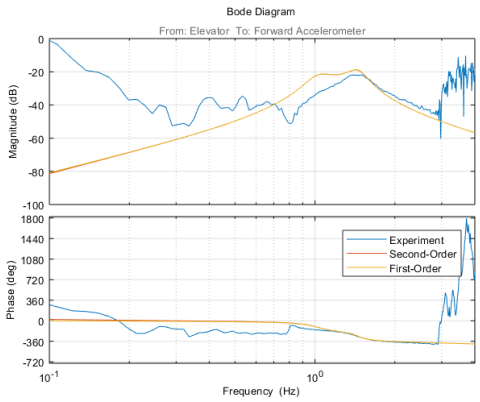

(a) Correction factor = 0.4.

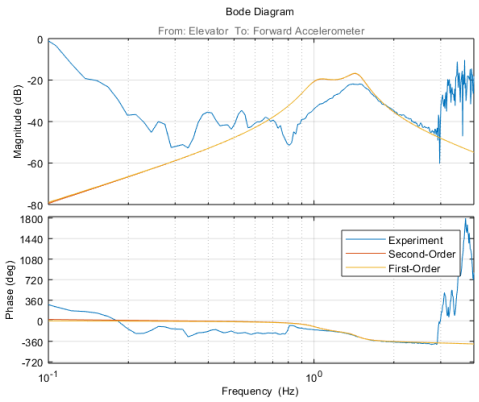

(b) Correction factor = 0.5.

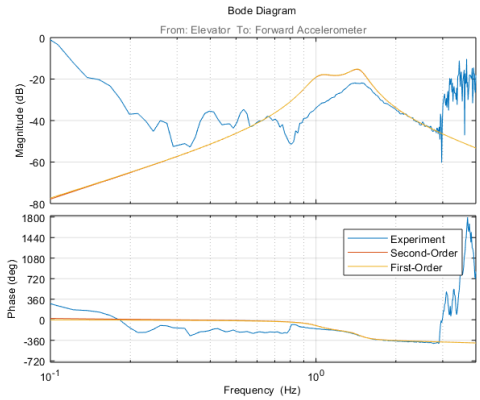

(c) Correction factor = 0.6.

Figure 6.3: Aerodynamic correction factors.

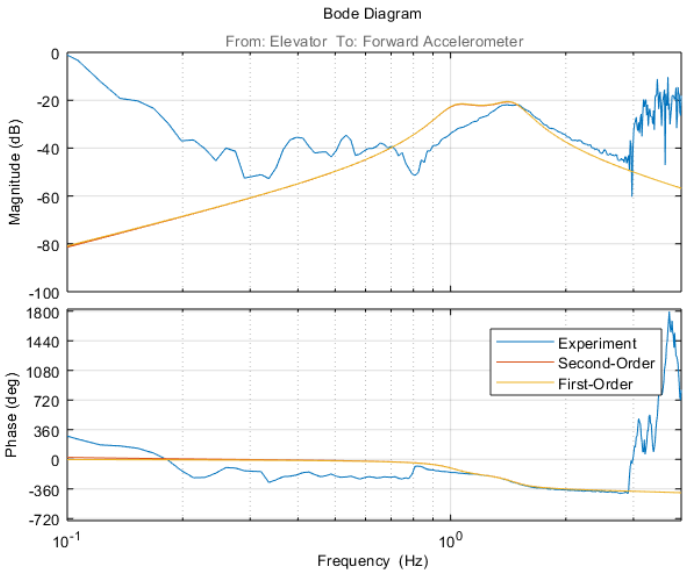

Figure 6.4: Added structural damping of $\zeta = 0.02$.

6.2.2 Structural Damping Effects

The effects of damping on the system can be determined by assessing the frequency response with varying values of ζ for the range that was determined from laser vibrometer testing. When this was done, the structural damping was found to be too small even for the highest value of the range, $\zeta = 0.02$, as seen in Figure 6.4.

The test article in its form installed in the tunnel has structural damping levels that are higher than what was measured on the wing in the lab. The wing tested in the lab pre-tunnel did not include any of the actuators or required wire for actuators and sensors. When the test article was installed in the tunnel, these were included in the wing. Cable bundles were passed between aerodynamic shells and bunched wires were interfering with the free vibration of the structure. This contributed to an increase in apparent structural damping.

Another consideration in the effects of the test article installation on the structural damping of

the system is the bearing used in the hanging sub-assembly. This bearing allows the model to have a pitch degree of freedom and ensure proper alignment of the test article. However, since the center of mass of the test article is not located directly in line with the bearing, there is some misalignment in the fore-aft direction. There is some friction that is associated with this misalignment in the bearing. This, then, appears in the experimental data as added structural damping that was not accounted for in the initial frequency response simulations.

Because of these effects, simulations were carried out for higher values of the structural damping ratio: $\zeta = 0.04, 0.06,$ and 0.08, as can be seen in Figure 6.5. A structural damping ratio of $\zeta = 0.04$ shows the closest match to the experimental results. Once the damping becomes greater than this, the system simulated is more damped than the experimental results show. Because this is not significantly higher than the pre-tunnel testing range and there are most likely factors that contributed to additional structural damping, a value of 0.04 is reasonable.

6.2.3 Hinge Friction Damping

The first element of the damping matrix used in the first-order method is associated with the damping of the hinge of the control surface. In simulations, this value has been zero; however, to capture the effects of the hinge friction, the value is made non-zero. Figure 6.6a shows the element being increased to a value 3.5 times that of the second diagonal element of the damping matrix. By increasing this damping value, the initial peak at 1 Hz more closely matches the expected trend. Since the second-order method uses artificial structural damping in lieu of the damping matrix, it is unaffected by these changes and therefore serves as a baseline for the fine-tuning prior to hinge friction effects.

Note that by increasing the value of hinge friction damping, the magnitude of the entire curve becomes slightly lower than the experimental data. When the $\{A_{sc}\}$ correction factor is increased from 0.4 to 0.6, the trend again falls more in line with the experimental data, as seen in Figure 6.6b Since typical values can range and 0.4 was at the low end of the range and values closer to 1 are

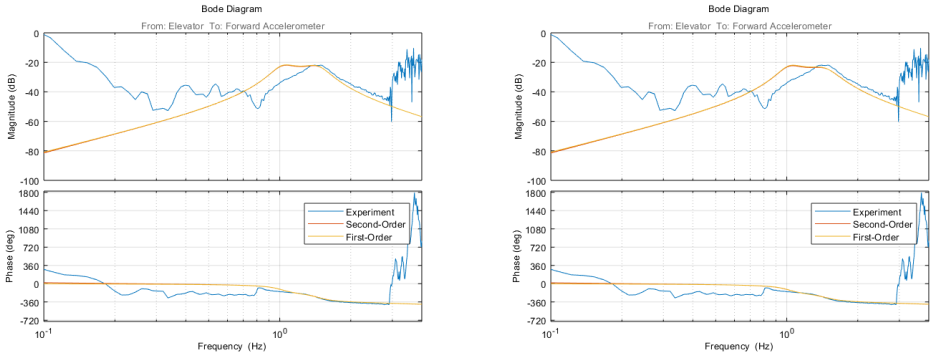

(a) Added structural damping of $\zeta = 0.04$. (b) Added structural damping of $\zeta = 0.06$.

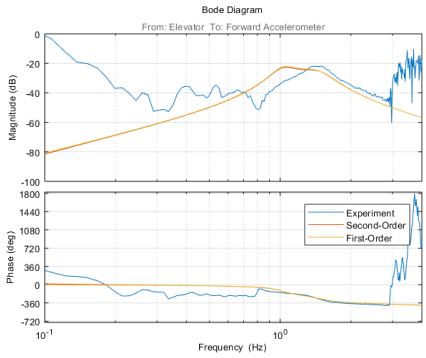

(c) Added structural damping of $\zeta = 0.08$.

Figure 6.5: Responses with varying added structural damping.

most reasonable, this increase is justified.

6.3 Additional Comparisons

6.3.1 Unsteady vs. Quasi-steady

Another interesting comparison from an aerodynamic prospective is between aeroservoelastic models based on the unsteady Doublet Lattice Method (DLM) and simulations based on quasi-steady

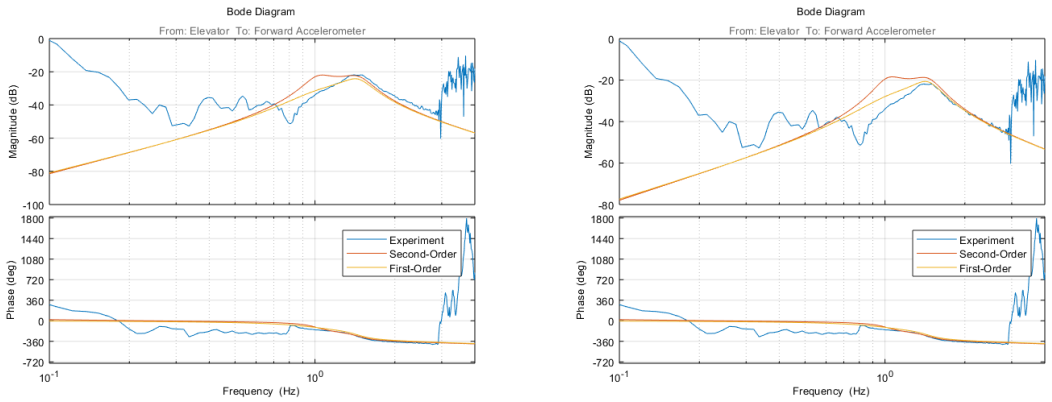

(a) With $\{A_{sc}\}$ correction of 0.4.

(b) With $\{A_{sc}\}$ correction of 0.6.

Figure 6.6: Effect of adding hinge friction damping.

aerodynamics [13]. As shown in Figure 6.7, the trend of the simulations done using an unsteady aerodynamic method match better than the simulation done using a quasi-steady method. This is to be expected since the unsteady method more accurately captures the unsteadiness of the flow. Still, the differences are not very high in the range of low frequencies studied here, and they are expected to be more pronounced over a wider range of frequencies extending to high frequencies.

6.3.2 Ceiling Gap

All of the simulation - test comparisons discussed so far accounted for a gap that exists between the root of the test article and the ceiling of the wind tunnel. This gap is approximately 4.5 inches and affects overall model aerodynamics and control surface efficiency. The simulated frequency responses from the NASTRAN data modeled with a gap and without a gap are shown in Figure 6.8. Both of these simulations use the corrected $\{A_{sc}\}$ factor of 0.6, a hinge friction damping factor of 3.5, and a damping ratio of $\zeta = 0.04$.

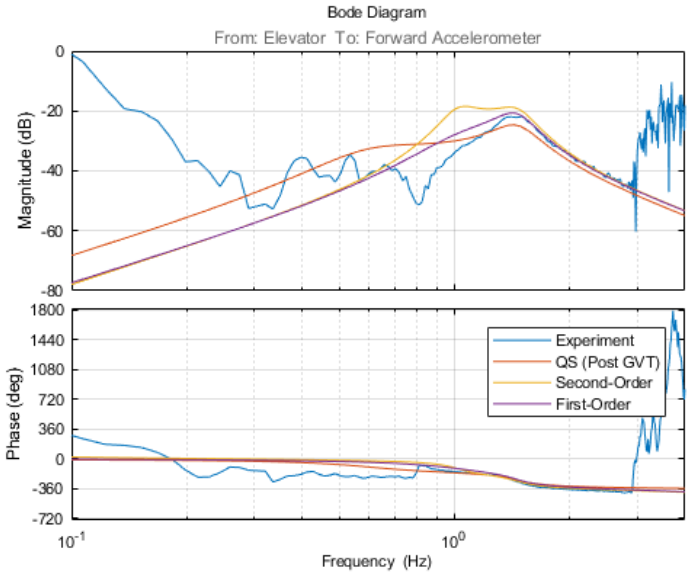

Figure 6.7: Comparison of simulations done using different methods of aerodynamic analysis.

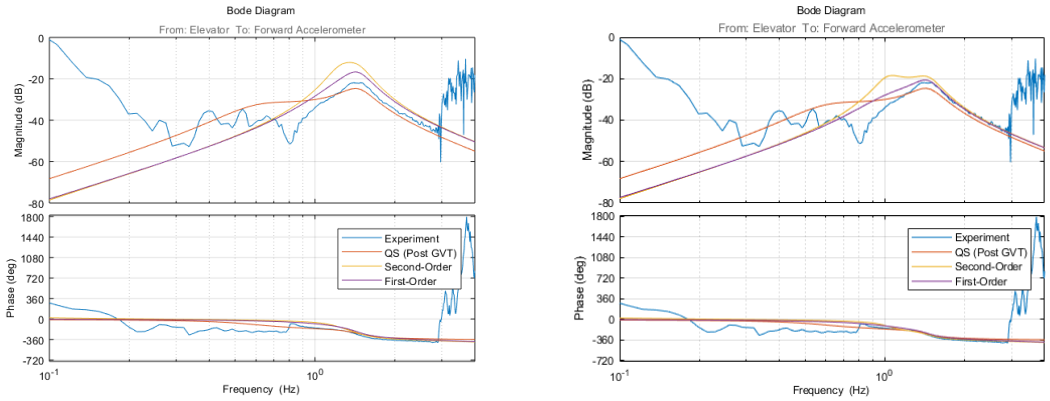

(a) Without ceiling gap.

(b) With ceiling gap.

Figure 6.8: Effect of addition of ceiling gap in simulated data.

6.4 Other Observations

6.4.1 Short Period

The short period captured by the simulation, based on the uncorrected NASTRAN model, is around 1 Hz. In the tunnel it was hard to capture by the wing-tip accelerometers, not surprisingly because of their short distance from the model hinge line, and was better captured by the Hall Effect Sensor. The simulation shows a response peak at around 1 Hz. The accelerometer, acting as a high pass filter, cannot be trusted below 1 Hz (see Figure 6.9). With higher and higher structural damping values, the short period peak in the frequency response, gets suppressed.

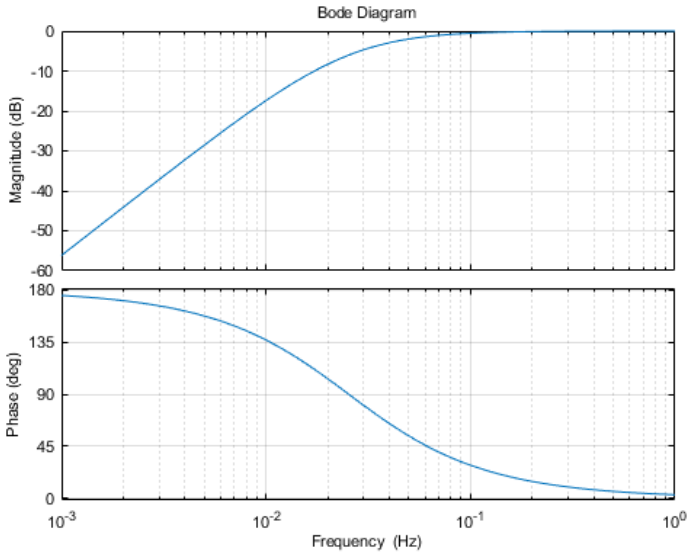

Figure 6.9: Accelerometer transfer function.

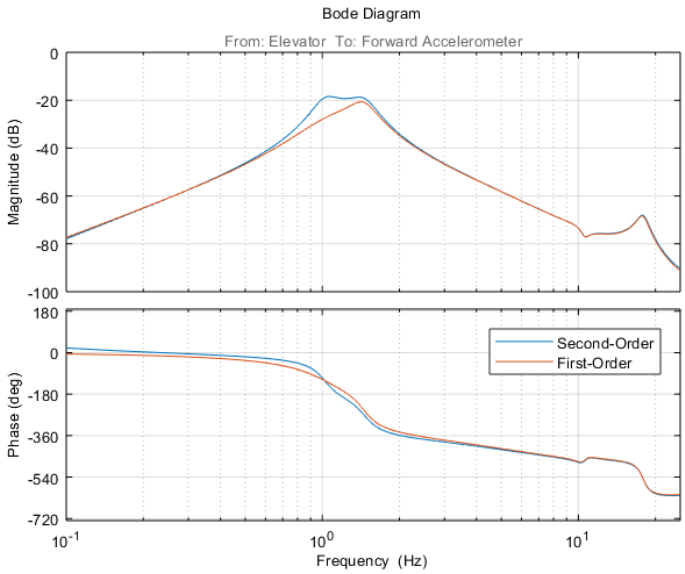

Figure 6.10: Frequency response up to 25 Hz.

6.4.2 Low Frequency Modes

Although the experimental results, because of the limitations of the test system, only focus on frequencies below 4 Hz , the frequency response can be simulated up through higher frequencies using both the second-order and first-order methods. The prediction of this extended range of low frequency modes is shown in Figure 6.10 up to 25 Hz. With better actuation used for models based on the model tested here, aeroservoelastic behavior over wider frequency bands will, hopefully, be tested in the future.

Chapter 7

CONCLUSION

Frequency response simulations of an elevator input to an accelerometer output using two different methods were developed and their results were compared to experimental data. After some adjustments for aerodynamic and structural effects, the results of both a second-order and first-order frequency response method showed good correlation to experimental data overall. The simulation models are based on an unsteady aerodynamic modeling method, which more accurately capture the physics of the problem and include adjustments that are derived from known physical effects. Experience in identifying modeling uncertainties and the way to address them in simulations has been gained.

While these simulations and comparisons include a great deal of work, there is still work that should be done to aid in developing AFS. The current simulation capabilities allow for varying input/output combinations. Other combinations, such as elevator to HES in the pitch degree of freedom, can be compared to the existing experimental data to gain more insight to the accuracy of the simulation and use of unsteady vs. quasi-steady aerodynamic techniques.

In addition to other input/output combinations, the simulation would benefit from the inclusion of effects of an external input such as gust. The incorporation of this into the simulations would enhance control law design capabilities. Finally, with confidence in math modeling and with experience in designing and testing gust load alleviation control laws, the next natural step would be the synthesis of control laws for active flutter suppression and their testing.

BIBLIOGRAPHY

[1] E. Livne, "Aircraft active flutter suppression: State of the art and technology maturation needs," *Journal of Aircraft*, vol. 55, no. 1, pp. 410–452, 2018.

[2] J. D. Quenzer, A. Zongolowicz, K. A. Hinson, B. Barzgaran, E. Livne, M. Mesbahi, and K. Morgansen, "Model for aeroelastic response to gust excitation," in *AIAA Scitech Forum*, 2019.

[3] B. Barzgaran, J. Quenzer, A. Zongolowicz, K. Hinson, M. Mesbahi, K. Morgansen, and E. Livne, "Low-cost wind tunnel studies of gust alleviation control techniques," in *International Forum on Aeroelasticity and Structural Dynamics*, 2019.

[4] D. Tang, P. G. A. Cizmas, and E. H. Dowell, "Experiments and analysis for a gust generator in a wind tunnel," *Journal of Aircraft*, vol. 33, no. 1, pp. 139–148, 1996.

[5] P. G. A. Cizmas, D. Tang, and E. H. Dowell, "Flow about a slotted cylinder-airfoil combination in a wind tunnel," *Journal of Aircraft*, vol. 33, no. 4, pp. 716–721, 1996.

[6] D. Tang and E. H. Dowell, "Experimental and theoretical study of gust response for high-aspect-ratio wing," *AIAA Journal*, vol. 40, no. 3, pp. 419–429, 2002.

[7] D. Tang, J. K. Henry, and E. H. Dowell, "Nonlinear aeroelastic response of delta wing to periodic gust," *Journal of Aircraft*, vol. 37, no. 1, pp. 155–164, 2000.

[8] C. Poussot-Vassal, F. Demourant, A. Lepage, and D. Le Bihan, "Gust load alleviation: Identification, control, and wind tunnel testing of a 2-d aeroelastic airfoil," *IEEE Transactions on Control Systems Technology*, vol. 25, no. 5, pp. 1736–1749, 2017.

[9] P. M. G. J. Lancelot, J. Sodja, N. P. M. Werter, and R. De Breuker, "Design and testing of a low subsonic wind tunnel gust generator," *International Forum on Aeroelasticity and Structural Dynamics*, 2015.

[10] J. Neumann and H. Mai, "Gust response: Simulation of an aeroelastic experiment by a fluid-structure interaction method," *Journal of Fluids and Structures*, vol. 38, pp. 290–302, 2013.

[11] Y. Babbar, V. S. Suryakumar, and T. W. Strganac, "Experiments in aeroelastic response and control under gust," in *54th AIAA/ASME/ASCE/AHS/ASC Structures, Structural Dynamics, and Materials Conference*, American Institute of Aeronautics and Astronautics, apr 2013.

[12] G. Platanitis and T. W. Strganac, "Suppression of control reversal using leading- and trailing-edge control surfaces," *Journal of Guidance, Control, and Dynamics*, vol. 28, pp. 452–460, may 2005.

[13] J. D. Quenzer, *Tools and Methods Toward the Advancement of Flight Control for Flexible Aircraft*. phdthesis, University of Washington, Seattle, Washington, Mar. 2019. Chapter 6.

Appendix A

SIMULATION FLOWCHART

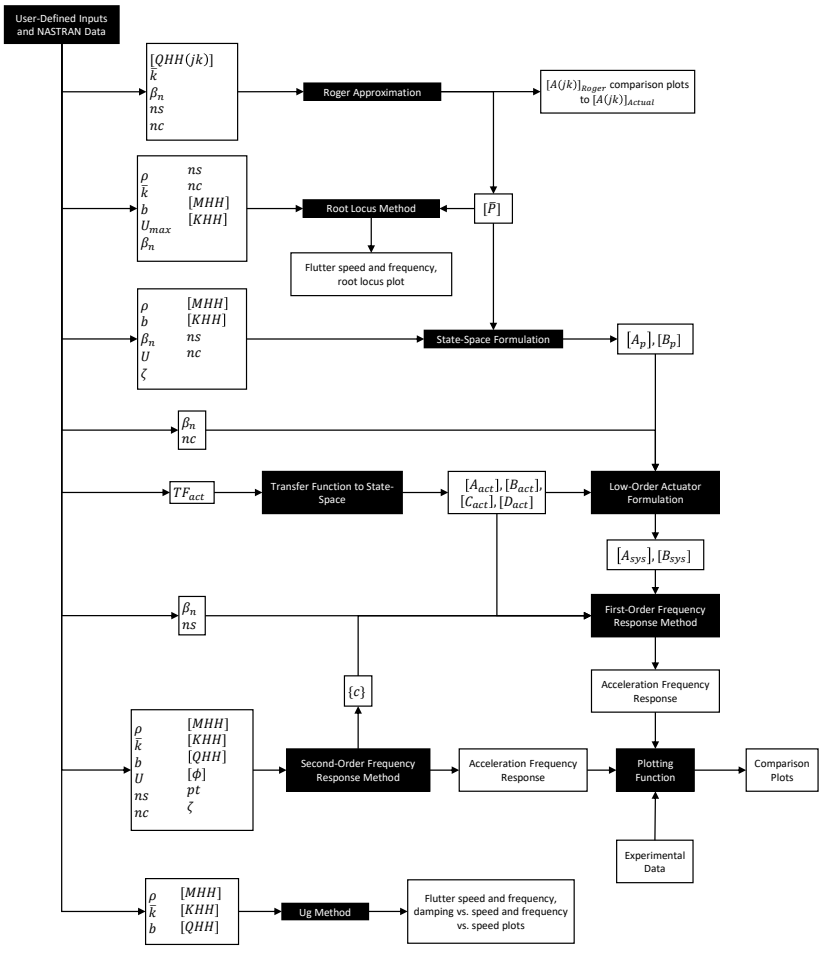

Figure A.1: Flowchart of MATLAB simulation.

Appendix B

FLUTTER PREDICTION METHODS

B.1 Ug Method

The U-g method for determining the flutter works with aerodynamic matrices for simple harmonic motion provided over a range of reduced frequencies: $[A(jk)]$. For this case, the NASTRAN data extracted included aerodynamic matrices at given tabulated reduced frequencies. In order to obtain a good enough resolution, the aerodynamic matrices required interpolation for reduced frequencies between those extracted from NASTRAN.

The process for finding the flutter point is derived from the equations of motion for simple harmonic motion.

$$\left[-\omega^2[M] + j[G_{st}][K] + [K] - q_d[A(jk)]\right]\{q(j\omega\} = \{0\} \tag{B.1}$$

where

$$[G_{st}] = \begin{bmatrix} g_{st_1} & 0 & \dots & 0 \\ 0 & g_{st_2} & \dots & 0 \\ \vdots & \vdots & \ddots & \vdots \\ 0 & 0 & \dots & g_{st_n} \end{bmatrix} \tag{B.2}$$

By defining

$$[\bar{K}] = [j[G_{st}][K] + [K]] \tag{B.3}$$

$$= [[1] + j[G_{st}]][K] \tag{B.4}$$

equation (B.1) becomes

$$\left[-\omega^2[M] + [\bar{K}] - q_D[A(jk)]\right]\{q(j\omega)\} = \{0\} \tag{B.5}$$

Again, because these aerodynamic forces are only for simple harmonic motion, it is assumed that oscillation of the simple harmonic motion nature is obtained after artificial structural damping is added to the system. This artificial structural damping is denoted g. Dividing equation (B.5) by ω^2 and noting that $\omega = Uk/b$,

$$\left[-[M] + \frac{1+jg}{\omega^2}[\bar{K}] - \frac{0.5\rho b^2}{k^2}[A(jk)]\right]\{q(j\omega)\} = \{0\} \tag{B.6}$$

Therefore,

$$\left([\bar{A}(k)] - \lambda[\bar{B}]\right)\{q\} = \{0\} \tag{B.7}$$

where

$$[\bar{A}(k)] = \left[-[M] - \frac{0.5\rho b^2}{k^2}[A(jk)]\right] \tag{B.8}$$

$$[\bar{B}] = -[\bar{K}] \tag{B.9}$$

and

$$\lambda = \frac{1+jg}{\omega^2}. \tag{B.10}$$

Since (B.7) is a generalized complex eigenvalue problem, the eigenvalues, λ, can be easily solved for. The eigenvalues are complex and therefore consist of a real and an imaginary part. From the definition of the eigenvalues in equation (B.10),

$$\text{Re}(\lambda) = \frac{1}{\omega^2} \tag{B.11}$$

$$\text{Im}(\lambda) = \frac{g}{\omega^2} \tag{B.12}$$

So,

$$g = \frac{\text{Im}(\lambda)}{\text{Re}(\lambda)} \tag{B.13}$$

$$\omega^2 = \frac{1}{\text{Re}(\lambda)} \tag{B.14}$$

Therefore, g and ω values can be found for each reduced frequency. Each reduced frequency and radial frequency also relate to a specific flight speed. The g and ω are plotted separately vs. the flight speed. The plot of the artificial structural damping and the plot of the frequency display branches. When the artificial structural damping is negative, energy must be taken from the system for simple harmonic motion to be occurring. When the damping is positive, it means that energy is being added to the system to keep it in simple harmonic motion, and so this is indicative of the system becoming unstable. So, when a branch on the plot crosses the x axis (the speed axis), the flutter point has been reached. The damping at which the branch crosses zero is interpolated and the flutter speed and correlating frequency are found.

B.2 Root Locus Method

The root locus method uses the plant matrix of the state-space representation to find the flutter speed. This matrix can be seen in equation (2.48). This matrix is found over a range of flight speeds that are determined from the tabulated reduced frequencies to make sure that no reduced frequency is higher than the highest reduced frequency for which unsteady aerodynamic forces have been provided.

$$k = \frac{\omega b}{U} \tag{B.15}$$

The eigenvalues of this $[A_p]$ matrix are found. They are real or complex. In the complex value case they have a real and imaginary part.

$$\lambda_i = \sigma_i + j\omega_i \tag{B.16}$$

The imaginary part is plotted vs. the real part and the results is a root locus plot in which branches appear. When one of the branches crosses the imaginary axis the system becomes unstable. By finding the flutter speeds and frequencies associated with the eigenvalue immediately before and after the branch crosses the imaginary axis, the flutter speed and frequency can be interpolated to find the exact point at which flutter occurs.